ISPRS Journal of Photogrammetry and Remote Sensing 228 (2025) 648–665

Contents lists available at ScienceDirect

ISPRS Journal of Photogrammetry and Remote Sensing

journal homepage: www.elsevier.com/locate/isprsjprs

Automatic in-situ radiometric calibration of TLS: Compensating distance and angle of incidence effects using overlapping scans

H. Laasch [a,*], T. Medic [a], N. Pfeifer [b], A. Wieser [a]

[a] Institute for Geodesy and Photogrammetry, ETH Zürich, Stefano-Franscini-Platz 5, 8093, Zürich, Switzerland
[b] Department for Geodesy and Geoinformation, TU Wien, Wiedner Hauptstrasse 8, 1040, Wien, Austria

ARTICLE INFO

Keywords:
LiDAR
Laser scanning
Intensity
Radiometric calibration
Remote sensing
Segmentation

ABSTRACT

Terrestrial laser scanners (TLS) commonly record intensity of the backscattered signal as an auxiliary measurement, which can be related to material properties and used in various applications, such as point cloud segmentation. However, retrieving the material-related information from the TLS intensities is not trivial, as this information is overlayed by other systematic influences affecting the backscattered signal. One of the major factors that needs to be accounted for is the measurement configuration, which is defined by the instrument-to-target distance and angle of incidence (AOI). By obtaining measurement-configuration independent intensity (I_{MCI}) material probing, classification, segmentation, and similar tasks can be enhanced. Current methods for obtaining such corrected intensities require additional dedicated measurement set-ups (often in a lab and with specialized targets) and manual work to estimate the effects of distance and AOI on the recorded values. Moreover, they are optimized only for specific datasets comprising a small number of targets with different material properties. This paper presents an automated method for in-situ estimation of I_{MCI}, eliminating the need for additional dedicated measurements or manual work. Instead, the proposed method uses overlapping point clouds from different scan stations of an arbitrary scene that are anyway collected during a scanning project. We demonstrate the generalizability of the proposed method across different scenes and instruments, show how the retrieved I_{MCI} values can improve segmentation, and how they increase the comparability of the intensities between different instruments.

1. Introduction

Terrestrial laser scanning (TLS) involves measuring the intensity of the backscattered signal as an auxiliary observation, which provides insights into material properties and surface conditions of the scanned objects (e.g. Han et al. (2022) and Errington et al. (2016)). For example, estimating the humidity of an object from the recorded intensities was demonstrated in a number of studies, e.g. Kaasalainen et al. (2010), Tan et al. (2020), Jin et al. (2021), and Laasch et al. (2023). In addition to the characterization of the material properties and related surface conditions, using intensities as additional observations allows for more accurate classification and segmentation, and it enhances LiDAR-inertial odometry (Harintaka and Wijaya, 2024; Li et al., 2024; Maru et al., 2023; Viswanath et al., 2023; Pfreundschuh et al., 2024).

However, the intensity of the laser beam backscatter is not only defined by the material and its surface conditions, but also by the measurement configuration, instrument characteristics, and atmospheric conditions (Pfeifer et al., 2008). These further influences can be superimposed on the signal of interest and hamper the usefulness of directly recorded (raw or unprocessed) intensities, especially when the data are obtained using different measurement configurations or different instruments. Mitigating the impacts of these further influences is thus important when using the intensities for the above tasks, which relate to material and surface conditions. For this purpose, numerous studies have focused on understanding these effects and have developed methods to model and isolate them. In TLS, the impact of measurement configuration, which is defined by the angle of incidence (AOI) and range, has been identified as the primary source of interference, receiving the most scientific focus.

Investigating and modeling the relationship between the intensity and measurement configuration was initially tackled more than a decade ago, starting with the works of Pfeifer et al. (2007) and Kaasalainen et al. (2005), but is still not fully resolved, see e.g. Kashani et al. (2015) and Sanchiz-Viel et al. (2021). One reason is that no method can provide a generally applicable solution through rigorous a-priori laboratory radiometric calibration as the intensity-AOI relationship strongly depends on the material properties and surface

* Corresponding author.
E-mail address: laaschh@ethz.ch (H. Laasch).

https://doi.org/10.1016/j.isprsjprs.2025.07.012
Received 20 December 2024; Received in revised form 14 March 2025; Accepted 8 July 2025
Available online 7 August 2025

conditions (Carrea et al., 2016), and the variety of different surfaces found in practice cannot be adequately replicated in a laboratory setting. A bulk of research focused on the topic of such a-priori radiometric calibration (e.g. Elsherif et al. (2018), Tan and Cheng (2015), Maru et al. (2023), Li et al. (2024), Errington et al. (2015), and Wei Fang et al. (2015)), from which two main conclusions can be drawn: (a) good transferability of the intensity-range models across different scenes, given the measurements with a common instrument; (b) limited transferability of a-priori developed intensity-AOI models.

These realizations motivated shifting the research efforts partially to in-situ and data-driven methods or hybrid methods combining a-priori and in-situ solution. For example, relatively recent methods presented in Tan et al. (2019), Carrea et al. (2016) and Li et al. (2023), model one of the dependencies (either distance or AOI) using additional prior measurements, while estimating the second one in-situ. Although the presented methods were adequate for the particular case studies, they required manual work, lacked automation, and were developed and optimized for specific applications and datasets containing a small range of targets with different material and surface characteristics (often only one type). Hence, they were never meant to be generally applicable.

Motivated by the latter, we introduce herein a method for estimating measurement-configuration independent intensity values (I_{MCI}), without requiring manual work or additional a-priori calibration scans, while assuring the method's general applicability across various datasets and TLS instruments. To the best of our knowledge, this is the first attempt at obtaining such a generalizable data-driven in-situ method for retrieving the I_{MCI} from TLS intensities. We refer to the result of our in-situ radiometric calibration as I_{MCI} instead of reflectance, as estimating reflectance would require introducing additional materials (targets) of known reflectance within the scene, something that would limit the general applicability of our method. Moreover, by definition, reflectance is dependent on at least one angle describing the geometric relationship between the incoming laser beam and the target surface (incidence angle), while our aim is to derive representative values unrelated to measurement configuration, hence, I_{MCI}.

The proposed method exploits the overlap of the point clouds acquired from different scan stations that are collected anyway within typical large scanning projects (comprising more than only a handful of scans). As a prospective application, we demonstrate the benefit of using the obtained I_{MCI} instead of raw unprocessed intensities for point cloud segmentation. Furthermore, we investigate how using I_{MCI} increases the comparability of the recorded intensities between different instruments. In general, the proposed method aims to streamline the radiometric correction process, making it more efficient and applicable to diverse datasets, and useful for following downstream tasks.

The remainder of this paper is organized as follows: Section 2 provides the theoretical background and discusses related work. Section 3 details our automatic in-situ radiometric calibration method. The datasets used for the analysis are introduced in Section 4. Section 5 presents the results of our method, followed by the conclusions in Section 7.

2. Theoretical background and related work

This section is divided into two subsections. The first subsection defines the measurement-configuration independent intensity values (I_{MCI}), explaining their relationship to the received laser power and measured (raw) intensities. It also introduces all relevant terms necessary for understanding the proposed radiometric compensation method and interpreting the resulting values. The second subsection provides an overview of radiometric compensation methods and places the proposed method within this context.

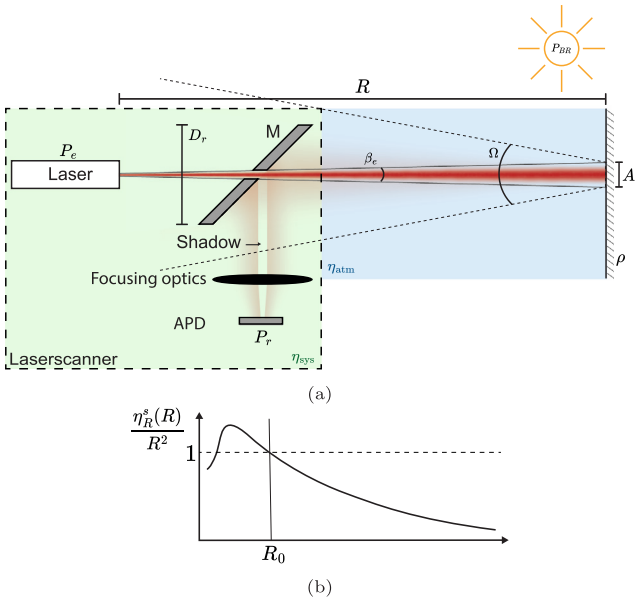

Fig. 1. Visualization of the parameters in the LiDAR equation and the near-range effect. (a) shows an illustration of a simplified laser beam propagation path with all elements influencing the received power according to Eq. (1). (b) shows the schematic illustration of the range dependence showing the near range effect of the system constant mixed with the quadratic decay. The range dependent effects are normalized to 1 for R_0. (APD - avalanche photodiode, M - mirror).

2.1. Definition of I_{MCI}

The LiDAR equation (Jelalian, 1992) as physical model, relates the received power of the laser beam to the emitted power as a function of various influencing factors. One such factor is the measurement configuration, the influence we aim to model and account for within this work. The LiDAR equation is given as:

$$P_r = \frac{P_e D_r^2}{4\pi\beta_e^2 R^4}\frac{4\pi A\rho}{\Omega}\eta_{\mathrm{Atm}}\eta_{\mathrm{Sys}} + P_{\mathrm{BR}} \tag{1}$$

The received power P_r depends on: the emitted power P_e, receiving aperture diameter D_r, beam divergence β_e, range to the measured object (i.e. target surface) R, illuminated area A, reflection coefficient of the target surface ρ, scattering solid angle of the target surface Ω, atmospheric transmission η_{Atm}, system transmission η_{Sys} and background radiation P_{BR} (see Fig. 1(a)).

Several simplifying assumptions can be made in the case of TLS measurements at typical ranges (a few tenths to a few hundred meters). It can be assumed that (i) the target is larger than the beam width, allowing the illuminated area to be expressed as $A = R^2\beta_e^2\frac{\pi}{4}$, and that (ii) the atmospheric transmission is 1 as it has a negligible influence on the above-mentioned measurement ranges (Bretagne et al., 2018). In this study, we additionally introduce assumption (iii), that the background radiation is also negligible. The latter is based on a personal communication with employees of Zoller+Fröhlich, according to which background radiation just causes a usually small increase of the noise level. With these assumptions, we can simplify Eq. (1) to:

$$P_r = \frac{P_e D_r^2 \pi\rho}{4\Omega R^2}\eta_{\mathrm{Sys}} \tag{2}$$

The system transmission η_{Sys}, that describes the system specific attenuation (i.e. scanner s specific attenuation), can be modeled with a constant η_c^s and a range dependent part $\eta_R^s(R)$:

$$\eta_{\mathrm{Sys}} = \eta_c^s \cdot \eta_R^s(R) \tag{3}$$

The separation is convenient as, at short distances, the attenuation due to the shadow of the laser beam exit hole in the mirror (see

Fig. 1(a)) falling onto the optical elements for collecting the reflected laser light (incl. avalanche photodiode, APD) is changing and is significantly larger than at long distances; and, in addition, the laser is deliberately defocused at shorter ranges so that the returning power is not too strong and harmful for the APD. These mechanisms make η_{Sys} partially range dependent, which becomes prominent at shorter ranges (see Fig. 1(b)). This holds for typical TLS architectures, as we have confirmed particularly for Zoller+Fröhlich instruments through personal correspondence. We can therefore convert Eq. (2) to:

$$P_r = \frac{P_e D_r^2 \eta_c^s}{4} \cdot \frac{\pi \rho}{\Omega} \cdot \frac{\eta_R^s(R)}{R^2}, \tag{4}$$

whereby we express each fraction as a constant or function:

$$P_{\text{r},j,k}^s = C^s \cdot F^{\text{mat}_j}(\varphi_{j,k}) \cdot G^s(R_{j,k}) \tag{5}$$

where s indicates the used scanner (e.g. brand, type, instrument), j the measured point, k the scanner station (i.e. location), φ the AOI and R, as before, the range to the measured point. The first term C^s is a constant for a given scanner s, if we assume that none of the related variables have other significant dependencies, such as time or temperature. This holds if given adequate care during scanning, e.g., sufficient warm-up period and large changes in atmospheric conditions. In general, this assumption is an oversimplification because, for example, changes in instrument temperature can affect the measurements (Janßen et al., 2021).

The second term F^{mat_j} describes the AOI dependent influences on P_r, which depend on the target's properties (incl. material *mat*) at the measured point j; and on the measurement configuration between j and the scanner location k through $\varphi_{j,k}$. The third term G^s describes the distance dependent influences, which are scanner specific and defined by the relative geometry between scanner station k and object point j through $R_{j,k}$. Hence, to obtain the measurement-configuration independent intensity values I_{MCI}, we need to find adequate functional approximations of the AOI dependent term F^{mat_j} and the range dependent term G^s for a given scanner s and eventually a given target material *mat*.

Regarding the AOI dependent term, for a single scanned point j on a Lambertian surface (we omit the indices for simplicity), $F^{\text{mat}}(\varphi)$ can be defined as (Lambert, 1760)

$$F^{\text{mat}}(\varphi) = \frac{\rho^{\text{mat}} \cdot \pi}{\Omega(\varphi)} = \rho^{\text{mat}} \cdot \cos\varphi \tag{6}$$

which combines a material dependent reflectance ρ^{mat} and the cosine-based AOI mapping function for Lambertian surfaces. However, most surfaces are not strictly Lambertian reflectors, and thus, require a more general representation of $F^{\text{mat}}(\varphi)$. Therefore, we rewrite Eq. (6) as

$$F^{\text{mat}}(\varphi) = \rho^{\text{mat}} \cdot f(\varphi) \tag{7}$$

where $f(\varphi)$ can take different forms corresponding to different reflection models (see Table 1). The choice of the suitable model, as well as its potential hyperparameters $a_1, \ldots, a_{N_f}$, depends on the target's material and surface conditions:

$$F^{\text{mat}}(\varphi) = \rho^{\text{mat}} \cdot f^{\text{mat}}(\varphi; a_1, \ldots, a_{N_f}) \tag{8}$$

In the above equation, as defined for a Lambertian surface, ρ^{mat} is the reflectance at the AOI $\varphi = 0$ and is predominantly *influenced by* and *representative of* the target's physical properties (e.g., humidity, spectral reflection properties, etc.). However, for specularly reflective materials, the reflectance is predominantly influenced by the surface conditions and the AOI φ (e.g., highly reflective shiny surface exhibiting strong reflection at small φ and a weak reflection at larger φ).

As the downstream tasks using I_{MCI} could focus on either of these two target related properties (surface or material), we introduce a tunable parameter φ_0 in the definition of F^{mat} as

$$F^{\text{mat}}(\varphi) = \rho^{\text{mat}} f^{\text{mat}}(\varphi_0) \cdot \frac{f^{\text{mat}}(\varphi)}{f^{\text{mat}}(\varphi_0)} =: \rho_{\varphi_0}^{\text{mat}} \cdot f_{\varphi_0}^{\text{mat}}(\varphi) \tag{9}$$

where $f^{\text{mat}}(\varphi_0)$ is a scalar value and serves as a scale factor. Here, $0 \leq \varphi_0 < 90°$ is a suitably chosen hyperparameter representing the AOI at which we define the (new) material or surface dependent coefficient of reflection $\rho_{\varphi_0}^{\text{mat}}$. In other words, φ_0 regulates the information content and meaning of parameter $\rho_{\varphi_0}^{\text{mat}}$.

From this definition (Eq. (9)), it follows that

$$f_{\varphi_0}^{\text{mat}}(\varphi_0) = 1. \tag{10}$$

Even after this modification (generalization), choosing $\varphi_0 = 0$ and choosing an appropriate $f^{\text{mat}}(\varphi)$ (a cosine-based mapping function) leads to the standard formulation for a Lambertian reflector as given in Eq. (6). However, choosing different functions and a different φ_0 allows us to better deal with situations where the reflection is non-Lambertian. In Section 3, we will introduce and explain our proposed choice of φ_0 and discuss further implications for non-Lambertian reflection.

For modeling the range dependent part of the LiDAR equation, we defined η_R^s/R^2 as $G^s(R)$ (the third term in Eqs. (4) and (5)). However, separating the system transmission into a constant and a range dependent part (Eq. (3)) is unique only up to a scaling factor of η_c^s and the inverse scaling of $\eta_R^s(R)$ (comparable to scaling/inverse-scaling introduced in Eq. (9)). Hence, in order to unambiguously define the separation, we need to somehow condition the value of the range dependent term $\eta_R^s(R)$ for some chosen range R_0 (see e.g. Fig. 1(a)). We thus impose

$$\eta_R^s(R_0) \overset{!}{=} R_0^2, \tag{11}$$

denote the corresponding function as $\eta_{R_0}^s(R)$, and define the function G, which now depends on R_0 as

$$G_{R_0}^s(R) := \frac{\eta_{R_0}^s(R)}{R^2}. \tag{12}$$

The true system transmission will typically not be known and needs to be approximated by a suitable function. Following the same approach as with the function F before, we subsequently represent $G(R)$ by g whose model and hyperparameters $b_1, \ldots, b_{N_g}$ have to be chosen or estimated with sufficient accuracy such that:

$$G_{R_0}^s(R) = g_{R_0}^s(R; b_1, \ldots, b_{N_g}). \tag{13}$$

These transformations of $G^s(R)$ have three consequences. First, the constant term η_c^s also depends on the choice of R_0, and we will subsequently indicate it as η_{c,R_0}^s. Second, the same holds for C^s (see Eq. (5)) because it includes η_c^s; we thus write $C_{R_0}^s$ subsequently. Finally, the condition introduced in Eq. (11) results in

$$g_{R_0}^s(R_0) = 1 \tag{14}$$

which effectively defines (fixes) the scale of the $G^s(R)$ outputs.

To approximate $\eta_{R_0}^s(R)$, no physical model is available, and therefore, various empirical models for $g_{R_0}^s(R_{j,k})$ have been explored in the literature. For example, Li et al. (2023) utilized a seventh-degree polynomial and an exponential function, defining the splitting point based on the first minimum of the discrete derivative of the distance-intensity relation. In contrast, Pfeifer et al. (2008) employed two linear functions, while Elsherif et al. (2018) used a combination of 2nd and 6th-degree polynomials with a splitting point at 4 m. Additionally, Sanchiz-Viel et al. (2021) and Bai et al. (2023) applied a 9th-degree polynomial function. To be more flexible, Errington et al. (2015) used third-order cubic splines for modeling the distance dependence. Hence, we implemented smoothing splines to be flexible and generalizable across different scanners and datasets (more in Section 3).

With the definitions of the AOI and distance dependence, Eq. (4) can be rewritten as follows:

$$P_{\text{r},j,k}^s = C_{R_0}^s \cdot f_{\varphi_0}^{\text{mat}_j}(\varphi_{j,k}) \cdot g_{R_0}^s(R_{j,k}) \cdot \rho_{\varphi_0}^{\text{mat}_j} \tag{15}$$

Table 1
Definition of f^{mat} for various established reflection models and additional ones, used later in this paper; the formulations have been adapted to the symbols used herein, and terms absorbed by ρ^{mat} or canceling because of the normalization according to Eq. (9) have been omitted.

Model	Abbrv.	$f^{\text{mat}}(\varphi) =$	
Lambertian (Lambert, 1760)	L	$\cos\varphi$	[a]
Lambert–Beckmann (Poullain et al., 2012)	LB	$\cos\varphi + a_1 \cdot \frac{e^{-\tan^2\varphi/a_2^2}}{\cos^5\varphi}$	[a]
Lommel–Seeliger–Lambert (Kaasalainen et al., 2011)	LSL	$\cos\varphi + a_1 \cdot \cos^2\varphi$	[a]
Blinn–Phong (Blinn, 1977)	BP	$\cos\varphi + a_1 \cdot \cos^{a_2}\varphi$	[a]
Oren–Nayar (Oren and Nayar, 1994)	ON	$\cos\varphi \cdot (1 - \frac{0.5 \cdot a_1^2}{a_1^2+0.33} + \frac{0.45 \cdot a_1^2}{a_1^2+0.09} \sin\varphi \tan\varphi)$	[a]
Adapted Lambertian	AL	$\cos\varphi + a_1$	
Smoothing Splines (Dierckx, 1975)	SS	$\sum_{j=1}^{n} a_j \cdot h_j(\varphi)$ (h_j is a cubic polynomial function)	
Adapt. Lamb. & Sm. Spl.	AL+SS	same as SS, but with AL as initialization step	

[a] Models have already been used in the literature to compensate the AOI effects in TLS intensity.

This equation shows the relationship between the received power P_r and the reflectance coefficient $\rho_{\varphi_0}^{\text{mat}_j}$, which is the ultimate value of interest and the value we want to approximate by our I_{MCI}. We could thus calculate $\rho_{\varphi_0}^{\text{mat}_j}$ —as an indication of the respective material—for each point in a point cloud from the received power, if the scanner constant C, as well as the models and hyperparameters (not shown here for simplicity) of f and g are known. The latter can be achieved, as will be described in Section 3.

However, typical instruments do not output the received power, but instead assign an intensity value I to each point in the point cloud. This intensity is related to the received power by a function $\mathcal{I}^s$ depending on the scanner's detector hardware (including e.g., the selected APD) and algorithmic choices made by the manufacturer. We can formally express this as

$$I_{j,k}^s = \mathcal{I}^s(P_{\text{r},j,k}^s). \tag{16}$$

Manufacturers typically do not disclose this function. However, Pfeifer et al. (2008) showed that $\mathcal{I}^s$ can be expressed as:

$$I_{j,k}^s = \gamma^s \cdot P_{\text{r},j,k}^s. \tag{17}$$

or

$$I_{j,k}^s = \gamma^s \cdot \log_{10} P_{\text{r},j,k}^s, \tag{18}$$

i.e., a linear or logarithmic function with a scale parameter γ^s, which models the relationship with sufficient accuracy for a large range of received powers. More complex relationships probably exist, e.g., if the scanner firmware applies a histogramm-based adaptation of the intensity values of each individual scan. However, herein, we assume the linear relationship according to Eq. (17) for the following equations (confirmed, e.g., for the Zoller+Fröhlich scanners used within the study through personal correspondence with the manufacturer). In practice, it is possible to distinguish if a scanner has a logarithmic or a linear relationship by measuring multiple targets with different known reflectance values at a fixed range R and AOI φ, and subsequently by modeling the observed $I_{j,k}^s$ vs. $\rho_{\varphi_0}^{\text{mat}_j}$ relationship; and in the case of recognizing a logarithmic relation between power and intensity, it is still possible to use the linear model by applying appropriate transformations of $I_{j,k}^s$ (e.g. by substituting $I_{j,k}^s$ with $10^{I_{j,k}^s}$). Hence, the following equations can be considered universally applicable.

By combining the Eqs. (15) and (17) the (desired) reflectance values can now be related to the actually available intensity values as follows:

$$I_{\text{r},j,k}^s = \kappa_{R_0}^s \cdot f_{\varphi_0}^{\text{mat}_j}(\varphi_{j,k}) \cdot g_{R_0}^s(R_{j,k}) \cdot \rho_{\varphi_0}^{\text{mat}_j} \tag{19}$$

where the original scanner constant C_s is extended by the intensity scaling factor γ^s:

$$\kappa_{R_0}^s = \gamma^s \cdot C_{R_0}^s \tag{20}$$

Under the assumption that downstream tasks like point cloud segmentation, classification or analysis of (changing) surface conditions can be accomplished using the reflectance values $\rho_{\varphi_0}^{\text{mat}_j}$ per point, the goal is now to calculate these values from the intensities I^s output by the scanner. This requires the scanner dependent constant $\kappa_{R_0}^s$, the model and hyperparameters of $g_{R_0}^s$, and the model and hyperparameters of $f_{\varphi_0}^{\text{mat}_j}$ to be known.

$\kappa_{R_0}^s$ and $g_{R_0}^s$ only depend on the scanner and do not change over time (given appropriate warm-up) unless the scanner's software or hardware changes, e.g., due to updates or repairs. Therefore their respective values could either be provided by the manufacturer, determined by the user or a service provider using special calibration measurements, or — under certain conditions — be estimated on-the-job by the user. The function $f_{\varphi_0}^{\text{mat}_j}$ does not depend on the scanner but depends on the measurement configuration (AOI) and on the scanned objects (material and surface conditions). It can thus (usually) not be determined beforehand but needs to be determined on the job. Exceptions would be applications, where the material and surface conditions are known, e.g., because only prefabricated elements are being scanned, and the functions determined earlier for the corresponding materials and surface conditions are usable for subsequent scans.

However, if the system constant $\kappa_{R_0}^s$ is not known, the scanned scene does not include any surfaces of known reflective properties (ρ^{mat_j} and f^{mat_j}), and the user does not have access to a reflectance standard (e.g., a Spectralon® target), $\rho_{\varphi_0}^{\text{mat}_j}$ cannot be determined using an on-the-job calibration. Despite that, many of the mentioned downstream tasks may be feasible also with an arbitrarily scaled version of ρ, in particular, if only one scanner or only scanners of the same brand and type are used. In this case, the product of the unknown system constant and the unknown coefficient of reflectance is treated as a single unknown which we denote as measurement configuration independent intensity I_{MCI} herein:

$$I_{\text{MCI},j,k}^s := \kappa_{R_0}^s \cdot \rho_{\varphi_0}^{\text{mat}_j}. \tag{21}$$

The $I_{\text{MCI},j,k}^s$ still represents the material and surface conditions, just in a scanner dependent way rather than independent of the scanner and is thus given by

$$I_{\text{MCI},j,k}^s = \frac{1}{f_{\varphi_0}^{\text{mat}_j}(\varphi_{j,k}) \cdot g_{R_0}^s(R_{j,k})} \cdot I_{\text{r},j,k}^s \tag{22}$$

If the manufacturer would provide the value of $\kappa_{R_0}^s$ and the related distance function $g_{R_0}^s(R)$, or distance independent intensities corresponding to $I_{\text{MCI},j,k}^s/(\kappa_{R_0}^s g_{R_0}^s(R))$, the user would only have to determine $f_{\varphi_0}^{\text{mat}}(\varphi)$ for all (relevant) surfaces in the scanned scene to then calculate $\rho_{\varphi_0}^{\text{mat}}$. Currently, manufacturers do not provide this information or not in sufficient detail. The practically best approach might thus be for the user to first determine $\kappa_{R_0}^s$ and $g_{R_0}^s(R)$ using appropriate calibration measurements, or have this done by a service provider. As stated above, $f_{\varphi_0}^{\text{mat}_j}(\varphi)$ can usually not be provided beforehand and needs to be determined on the job by the user. If $g_{R_0}^s(R)$ is not known and cannot be determined beforehand by calibration, it is also possible to choose functional models for $f_{\varphi_0}^{\text{mat}_j}(\varphi)$ and $g_{R_0}^s(R)$ and estimate their (hyper)parameters on the job simultaneously. Typically, this will be

the case when also κ is unknown and thus the calibration on the job is carried out to obtain I_{MCI} rather than $\rho^{\mathrm{mat}}_{\varphi_0}$. The method for such on-the-job calibration is introduced within this study and described in Section 3.

2.2. Overview of possible radiometric compensation methods

This subsection extends the overview of the radiometric compensation methods that were briefly introduced in the introduction, relates them to the terminology introduced in the previous section, and places the proposed compensation method within this context.

Kashani et al. (2015) propose categorizing LiDAR intensity compensation methods into levels, each indicating the degree of compensation applied to intensity values. At level 0, raw intensity values are used without compensation, while level 3 represents obtaining the "true" reflectance of the scanned surface. Intermediate levels are level 1, where intensity is compensated for AOI, distance, and other factors (or any subset of thereof), and level 2, where intensities are additionally transformed (e.g. scaled or shifted) to better align with neighboring scans. For the majority of the downstream applications (see Section 1), level 3 compensation provides the most suitable data representation. Relying on the terminology introduced in Section 2.1, level 3 compensation requires estimating three terms: $\kappa^s_{R_0}$, $f^{\mathrm{mat}_j}_{\varphi_0}(\varphi_{j,k})$, and $g^s_{R_0}(R_{j,k})$. These can be estimated through a laboratory, an in-situ or combined (partially lab and partially in-situ) compensation.

Laboratory compensation: In a laboratory setting, we can estimate $\kappa^s_{R_0}$ using a target with known reflectance $\rho^{\mathrm{mat}}_{\varphi_0}$, measured at a fixed AOI φ_0 and distance R_0. Varying the distance R while keeping the AOI constant enables estimating the function $g^s_{R_0}(R_{j,k})$. Such procedures were demonstrated in a number of publications, e.g. Tan and Cheng (2015), Wei Fang et al. (2015), and Sanchiz-Viel et al. (2021). The terms, $\kappa^s_{R_0}$ and $g^s_{R_0}(R_{j,k})$, are generally material independent and can be estimated during the instrument's factory calibration and provided by the TLS manufacturer. This is often the case, and the users have either access to both raw and such level 1 compensated intensities, or only to the latter. However, the specifics of the compensation procedure are typically not disclosed and the relation of the provided values to the level 3 compensated intensities is unclear.

The radiometric compensation for AOI related influence on intensities $f^{\mathrm{mat}_j}_{\varphi_0}(\varphi_{j,k})$ can be realized in two ways. The first one is to apply a single $f^{\mathrm{mat}_j}_{\varphi_0}(\varphi_{j,k})$ function to the entire point cloud. The second compensates each type of material within the point cloud using a material-specific function $f^{\mathrm{mat}_j}_{\varphi_0}(\varphi_{j,k})$. Tan and Cheng (2015), Maru et al. (2023), and Sanchiz-Viel et al. (2021) use a global AOI compensation function, typically determined in the laboratory with a reflectance standard. In these experiments, intensities are measured at different AOIs while the distance remains constant. In most cases, $f^{\mathrm{mat}_j}_{\varphi_0}(\varphi_{j,k})$ is estimated for predominantly diffuse materials, and the underlying assumption is that the majority of the materials found in our surrounding exhibit similar behavior (oversimplification).

For the material-specific AOI compensation, individual representative materials must be selected and measured in the lab, and the point cloud to be compensated has to be classified into these materials. This is laborious, but feasible for well-predefined and contained measurement tasks. Kaasalainen et al. (2011), for instance, focus on the material-specific AOI compensation of different materials such as sand, brick, concrete, and Gabbro rock.

Combined compensation: An alternative to the laboratory-only compensation is to estimate $f^{\mathrm{mat}_j}_{\varphi_0}(\varphi_{j,k})$ using the in-situ data, while $\kappa^s_{R_0}$ and $g^s_{R_0}(R_{j,k})$ are derived from laboratory experiments or provided by the manufacturer. A necessary requirement is sufficient distribution of AOI observations within the in-situ acquired point cloud, or its subset of interest. So far, such an approach was used only for material-specific estimation of $f^{\mathrm{mat}_j}_{\varphi_0}(\varphi_{j,k})$ where the subject of scanning was a single clearly predefined target with homogeneous reflectance properties (e.g. Li et al. (2023)). However, the combined compensation could also be realized by estimating a single global AOI compensation function that best approximates the radiometric behavior of the entire scene, or expanded to estimating material-specific AOI functions for all materials that can be recognized and (automatically) segmented within the point cloud.

In-situ compensation: To estimate all three terms solely from in-situ data, the dataset must include sufficient distribution of measured distances and AOIs, but also fulfill the following condition: the distributions of distances, AOIs and reflectance values have to be sufficiently uncorrelated to allow for unambiguous estimation of each targeted term. On top of that, the scene should entail one or more objects with known reflectance to allow for estimating $\kappa^s_{R_0}$. In reality, these are general requirements for reaching level 3 radiometric compensation, but in the previous cases the difficulty of achieving it is significantly reduced by incorporating lab-procedures with dedicated measurement configurations and targets of known reflectance. One viable way of tackling this problem in-situ would be replicating the strategy of the combined compensation as discussed above, but realized fully on site, using any in-situ available target of known or unknown reflectance for replicating laboratory-based part of the procedure to estimate $g^s_{R_0}(R_{j,k})$ and eventually $\kappa^s_{R_0}$. Again, an additional challenge arises as, in the ideal case, $f^{\mathrm{mat}_j}_{\varphi_0}(\varphi_{j,k})$ has to subsequently be resolved separately for each material found in the scene. Such an approach is likely to be time-consuming due to the requirement of additional dedicated measurement configurations, or could even be unfeasible due to the measurement configuration constraints found on site.

Herein, we propose an alternative approach that leverages the commonly realized high overlap between the scans acquired within a single scan project, alleviating some of the latter concerns related to efficiency and to coupling of variables. The principle of the approach works as follows. Within smaller subsets of the mentioned scan overlaps, herein called patches, we can assume constant reflectance properties and use this assumption to estimate the reflectance values as unknowns in the system of equations. This assumption implies that the ratio of intensities of points within the same path only depends on the respective AOIs and distances but not on the reflectance. To achieve this, each patch must contain points from at least two point clouds with sufficiently different AOIs and distances. The more point clouds covering a patch with different AOIs and distances, the better we can resolve reflectance independently of distance or AOI. Consequently, each patch contains a quasi-random subsample of different AOIs and distances, which is essential for estimating and decoupling the targeted terms, thereby serving as a piece-wise solution to $g^s_{R_0}(R_{j,k})$ and $f^{\mathrm{mat}_j}_{\varphi_0}(\varphi_{j,k})$. Hence, after resolving for reflectance, we can combine the data of all such patches, and subsequently resolve for globally best-fitting $g^s_{R_0}(R_{j,k})$ and $f^{\mathrm{mat}_j}_{\varphi_0}(\varphi_{j,k})$ or even for material-specific $f^{\mathrm{mat}_j}_{\varphi_0}(\varphi_{j,k})$, given a-priori material segmentation of point clouds into different material-related classes.

Although most TLS datasets exhibit significant overlaps between scans from different stations, they often lack objects with known reflectance. In such cases, intensity compensation can only be realized up to the level 1, resulting in I_{MCI} (see Eq. (22)), and not up to the level 3. Nevertheless, for many downstream applications (see Section 1) working with I_{MCI} values is sufficient. Hence, in the following section, we present our method for automatic in-situ radiometric compensation of measured intensity values up to level 1.

3. Methods

The proposed method can be separated in two parts, which are presented in the following order: The first part is named "global compensation method" and aims at estimating the globally best-fitting $g^s_{R_0}(R_{j,k})$ and $f^{\mathrm{mat}_j}_{\varphi_0}(\varphi_{j,k})$ for the entire dataset. It has no extra requirements for the successful application besides the sufficient amount

and versatility of overlapping scans. The second part presents the subsequent expansion of the method necessary for estimating material-specific $f_{\varphi_0}^{\text{mat}_j}(\varphi_{j,k})$ terms. This part has an additional requirement of providing already semantically segmented point clouds, as will be elaborated in Section 3.2.

3.1. Global compensation method

3.1.1. Overview

As within the global compensation we estimate globally optimal terms for the entire scene, we estimate only one $f_{\varphi_0}^{\text{mat}_j}(\varphi_{j,k})$ as a mean for all present materials and call it $f_{\varphi_0}^{\text{glob}}(\varphi_{j,k})$. As mentioned, to solve for the terms, we exploit the overlap regions of point clouds acquired from several scanner stations. Although measurements from different scan stations do not sample exactly the same points in space, distances between the spatially nearest neighbor points of different stations are small given a sufficient scanning resolution. Therefore, we assume that neighboring points exhibit similar reflectance values and backscatter characteristics, as the material properties and surface conditions remain similar. This assumption and the existence of overlapping scans taken from multiple stations with varying measurement configurations (varying distances and AOIs) are the basis of the method.

To be able to handle large datasets and to estimate highly correlated parameters (assure convergence and numerical stability), we implemented an iterative estimation method that incorporates two convergence cycles (Hastie et al., 2009) following the initial point cloud processing (see Fig. 2). In the first cycle, the AOI and distance functions are estimated recursively. The second cycle contains the first one as its core part, it is initiated only after the 1st convergence of the 1st cycle, and is realized to estimate patch-wise normalization coefficients for the reflectance over the entire point cloud. By applying such reflectance normalization, we temporarily eliminate $\rho_{\varphi_0}^{\text{mat}_j}$ from the system of equations (Eq. (19)), allowing us to pool all data points together, irrespective of the material that they sampled, and use them simultaneously to estimate the globally optimal $f_{\varphi_0}^{\text{glob}}(\varphi_{j,k})$ and $g_{R_0}^{s}(R_{j,k})$ without a bias due to mixing of different materials.

The latter explanation is an oversimplification, as $\rho_{\varphi_0}^{\text{mat}_j}$ cannot be distinguished from $\kappa_{R_0}^{s}$ as long as $\kappa_{R_0}^{s}$ is unknown, and, hence, it cannot be directly eliminated from Eq. (19). Therefore, to facilitate the reflectance normalization, we introduce $\rho'^{\text{mat}_j}_{\varphi_0}$ and $\kappa'^{s}_{R_0}$, which are scaled by the mean reflectance of the entire point cloud:

$$\rho'^{\text{mat}_j}_{\varphi_0} = \frac{\rho_{\varphi_0}^{\text{mat}_j}}{\rho_{\varphi_0}^{\text{mean}}} \tag{23}$$

$$\kappa'^{s}_{R_0} = \kappa_{R_0}^{s} \cdot \rho_{\varphi_0}^{\text{mean}} \tag{24}$$

and by incorporating them into Eq. (19) we obtain:

$$I_{\text{r},j,k}^{s} = \kappa'^{s}_{R_0} \cdot f_{\varphi_0}^{\text{glob}}(\varphi_{j,k}) \cdot g_{R_0}^{s}(R_{j,k}) \cdot \rho'^{\text{mat}_j}_{\varphi_0} \tag{25}$$

Such modified $\rho'^{\text{mat}_j}_{\varphi_0}$ can be estimated in a data-driven way and be eliminated from Eq. (25) through the normalization (see subsection "Cycle 2"), while the $\kappa'^{s}_{R_0}$ is still a constant value that globally holds for the entire point cloud, hence, not influencing $f_{\varphi_0}^{\text{glob}}(\varphi_{j,k})$ and $g_{R_0}^{s}(R_{j,k})$ estimation.

To summarize, the proposed method has three main steps (point cloud processing, cycles 1 and 2), and three different terms are estimated within it: $f_{\varphi_0}^{\text{glob}}(\varphi_{j,k})$, $g_{R_0}^{s}(R_{j,k})$, and $\rho'^{\text{mat}_j}_{\varphi_0}$. The point cloud processing is done only once, while the cycles are repeated until the changes of the evaluated values of $f_{\varphi_0}^{\text{glob}}(\varphi_{j,k})$ and $g_{R_0}^{s}(R_{j,k})$, as well as of the normalization coefficients $\rho'^{\text{mat}_j}_{\varphi_0}$ for all points are below a manually defined threshold. The specific implementation details are given in the text below, and they follow the diagram of Fig. 2.

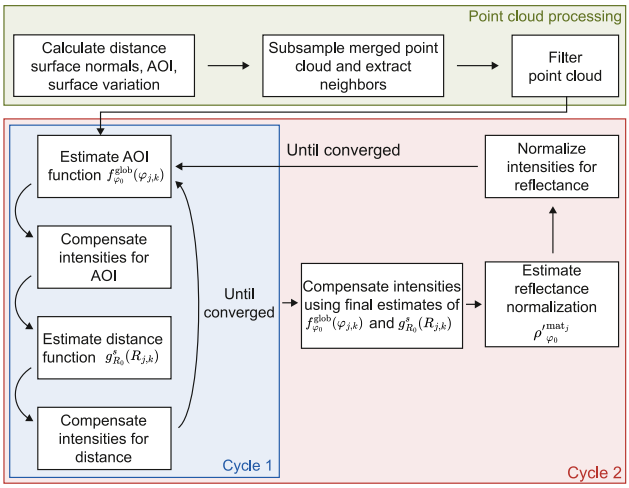

Fig. 2. Method of estimating the global AOI and distance function.

Point cloud processing

The necessary input for the method are separated point clouds of the individual scanner stations presented in a common coordinate system after point cloud registration, together with the corresponding information on scanner station poses. To filter the point cloud and initiate Cycle 1, the following attributes are extracted for each point:

- **Distance R:** the magnitude of the scanner station-to-point-vector.
- **Surface normals:** per-point estimated normal vectors of locally fitted planes within a certain radius around the query point.
- **AOI φ:** the angle between the scanner station-to-point vector and the corresponding surface normal.
- **Surface variation:** based on the PCA (principal component analysis) of the spherical neighborhood of a certain radius around the query point, according to Hackel et al. (2016).

Afterwards, the aligned point clouds of different scanner stations are processed together to establish common spatial patches with unique patch indices representing the spatial correspondence across the point clouds. The latter is realized as follows. A merged point cloud is spatially subsampled to the double of the patch radius, as these points are used as seed points for the patch assignment. All points of all original point clouds get clustered to a patch by nearest neighbor assignment with respect to the seed points. These patches are then used for computing the per-patch reflectance normalization coefficients $\rho'^{\text{mat}_j}_{\varphi_0}$ in Cycle 2.

Finally, only the points with a successfully estimated normal, a surface variation below a threshold, a distance smaller than the scanner's maximal range (according to specs sheets), and belonging to a patch containing points from at least three different stations are used for the following calculations in Cycles 1 and 2.

Remark. In our implementation of the proposed method, all (hyper-) parameter values are experimentally chosen to produce satisfactory results and generalize well across the datasets described in the following section. For example, for the computation of patch-wise reflectance normalization, we set the patch size to 5 cm radius as a trade-off between a sufficient number of points from multiple scan stations and the validity of the *consistent radiometric properties* assumption within the patch. The radius for computing the surface variation has the same size as the patches radii so that the surface variation values can better uncover the patches lying on surface edges (unwanted occurrence, explanation follows). The same radius of 5 cm is also used for the computation of surface normals so that the surface variation could in theory be used additionally as a measure of the

quality of the estimated normals (currently not exploited). We fixed the threshold for the filtering with the surface variation at 0.005 m, which we defined experimentally.

3.1.2. Cycle 1

In the first cycle (see Fig. 2), the point cloud points with the additional attributes are used to estimate $f^{\text{glob}}_{\varphi_0}(\varphi_{j,k})$ and $g^{s}_{R_0}(R_{j,k})$. The AOI-related function is estimated first, as the majority of the models we tested for approximating $f^{\text{glob}}_{\varphi_0}(\varphi_{j,k})$ are theoretical–empirical hybrid models (see e.g. Table 1) with lower flexibility and stronger regularization strength relative to purely empirical models for $g^{s}_{R_0}(R_{j,k})$. Hence, there is a much lower probability that during the first iteration $f^{\text{glob}}_{\varphi_0}(\varphi_{j,k})$ incorrectly "absorbs" and compensates for distance-related patterns in the data and leads to a solution only representing a local minimum, if the distance, AOI, and intensity are partially high correlated.

To estimate $f^{\text{glob}}_{\varphi_0}(\varphi_{j,k})$, we transform Eq. (25) to

$$\kappa'^{s}_{R_0} \cdot f^{\text{glob}}_{\varphi_0}(\varphi_{j,k}) = \frac{I^{s}_{\text{r},j,k}}{\rho'^{\text{mat}_j}_{\varphi_0} \cdot g^{s}_{R_0}(R_{j,k})}. \tag{26}$$

However, none of the variables besides $I^{s}_{\text{r},j,k}$ are known in the first iteration, requiring some mediation strategies. For $g^{s}_{R_0}(R_{j,k})$ and $\rho'^{\text{mat}_j}_{\varphi_0}$ we incorrectly assume that both are constant and equal to 1. We can only make this assumption in the case of a large data set (in this study this is $> 100'000'000$ points for each of the tested datasets) as we expect that, due to high variability in the values, neither the distances nor the reflectances are strongly correlated with the AOI values. $\kappa'^{s}_{R_0}$, on the contrary, must be estimated jointly with $f^{\text{glob}}_{\varphi_0}(\varphi_{j,k})$, but since $f^{\text{glob}}_{\varphi_0}(\varphi_{j,k})$ has the boundary condition (see Eq. (10)), it is possible to separate them.

We have set the condition at φ_0 to 0.3 rad because we wanted the reflectance values to be as representative as possible of "inner" material properties and be as independent as possible from the surface finish related properties, which dominate φ_0 values at both extrema, i.e. very high and very low AOIs (see Section 2.1). In practice, for estimating the $f^{\text{glob}}_{\varphi_0}(\varphi_{j,k})$ that best fits the entire dataset, the choice of the value is somewhat arbitrary, as the value is coupled with the scaling parameter $\kappa'^{s}_{R_0}$, which is unknown, and the choice of φ_0 just alters this scaling. However, the choice becomes relevant for the material dependent compensation described in Section 3.2.

Due to the large dataset, it is computationally expensive to implement estimation using all data points. Therefore, we average the distance-compensated and reflectance-normalized intensities (right side of Eq. (26)) in bins of 1 mrad across the entire AOI range and estimate the function $f^{\text{glob}}_{\varphi_0}(\varphi_{j,k})$ using these averaged data points (2d AOI-intensity value pairs). As the literature does not point out any functional model for $f^{\text{glob}}_{\varphi_0}(\varphi_{j,k})$ as the "best" or the most generalizable one, we tested common models from the literature plus three "custom-tailored" ones presented in Table 1. Regarding the additionally introduced models, the *adapted Lambertian* (AL) is based on the standard Lambertian model, but with an additional offset parameter a_1 allowing more flexibility. We also tested *smoothing splines* (SS) (Dierckx, 1975) due to their high flexibility as a representative of purely empirical models. Finally, we combined the *adapted Lambertian and smoothing splines* (AL+SS) to get a trade-off between high-flexibility and regularization strength of the theory-backed priors incorporated in the Lambertian model. This combination is realized by initially fitting the data to the AL model during the first convergence of Cycles 1 and 2, as an initialization step, and once both cycles converge, they are repeated with the SS model, using the previously estimated $g^{s}_{R_0}(R_{j,k})$ and $\rho'^{\text{mat}_j}_{\varphi_0}$.

For the estimation of $g^{s}_{R_0}(R_{j,k})$, we can introduce the adaptation of Eq. (25) that is directly comparable to the one done for $f^{\text{glob}}_{\varphi_0}(\varphi_{j,k})$ resulting in:

$$\kappa'^{s}_{R_0} \cdot g^{s}_{R_0}(R_{j,k}) = \frac{I^{s}_{\text{r},j,k}}{\rho'^{\text{mat}_j}_{\varphi_0} \cdot f^{\text{glob}}_{\varphi_0}(\varphi_{j,k})} \tag{27}$$

In this case, we can reduce the number of assumptions necessary in the first iteration, as we can now use the previously estimated $f^{\text{glob}}_{\varphi_0}(\varphi_{j,k})$ to adjust the raw intensity values. However, we still assume that $\rho'^{\text{mat}_j}_{\varphi_0}$ is equal to 1. For the implementation of this optimization step the data are averaged in 1 cm bins across the entire range of distance values to reduce the number of data points, and smoothing splines are used as the model for $g^{s}_{R_0}(R_{j,k})$ due to their flexibility, which was proven necessary in the previous works (see Section 1). Smoothing splines require only one hyperparameter, the smoothing factor, which we defined in a data-driven way based on the recommendations given in Dierckx (1975) by multiplying the number of binned data points (i.e. number of bins) with the variance of the binned data (in our case average of variances estimated with a moving window spanning through 20 bins - value experimentally chosen). Again, the function $g^{s}_{R_0}(R_{j,k})$ has the condition to be 1 at R_0 (see Eq. (14)). We chose 12.5 m to avoid the influence of the near range effects related to parameter $\eta_{\text{Sd}}(R)$ (see Eq. (3)) and to still maintain the I_{MCI} value range corresponding to higher I_{raw} values (e.g. we avoid setting R_0 to 100 m, which would effectively scale down all values with roughly 1/10,000 due to $1/R^2$ term in Eq. (12)).

Both functions $f^{\text{glob}}_{\varphi_0}(\varphi_{j,k})$ and $g^{s}_{R_0}(R_{j,k})$ are estimated with least squares, where the smoothing splines have an additional smoothness constraint. The cycle 1 is continuously repeated until the following convergence criterion is met: the median difference between the compensation factors (multiplied $f^{mat_j}_{\varphi_0}(\varphi_{j,k})$ and $g^{s}_{R_0}(R_{j,k})$ for each point) of the current and previous iterations must be less than 0.01, indicating that the remaining intensity value changes are within the roughly experimentally estimated noise level of approximately 1%.

3.1.3. Cycle 2

After $f^{\text{glob}}_{\varphi_0}(\varphi_{j,k})$ and $g^{s}_{R_0}(R_{j,k})$ are estimated, $I^{s}_{\text{MCI},j,k}$ can be calculated using Eq. (22). However, the estimates of both latter functions can be biased if different reflectance values $\rho^{\text{mat}_j}_{\varphi_0}$ of different materials are not accounted for, and if the spatial distribution of $\rho^{\text{mat}_j}_{\varphi_0}$ is accidentally correlated with the distributions of AOI or distance within the point clouds. Hence, in Cycle 2 we conduct the reflectance normalization using the term introduced in Eq. (23). For the normalization, we first need to estimate per patch $\rho'^{\text{mat}_j}_{\varphi_0}$ and use it as a normalization coefficient (scale factor), scaling the current estimates of $I^{s}_{\text{MCI},j,k}$ within each patch, making them reflectance independent. For estimating per patch $\rho'^{\text{mat}_j}_{\varphi_0}$ we assume that the reflectance within the patches is consistent. By averaging all current estimates of $I^{s}_{\text{MCI},j,k}$ within each patch and within the entire dataset ("all" for all points), it is possible to calculate $\rho'^{\text{mat}_j}_{\varphi_0}$ as:

$$\rho'^{\text{mat}_j}_{\varphi_0} = \frac{\rho^{\text{mean}}_{\varphi_0}}{\rho^{\text{mat}_j}_{\varphi_0}} = \frac{\kappa \cdot \rho^{\text{mean}}_{\varphi_0}}{\kappa \cdot \rho^{\text{mat}_j}_{\varphi_0}} = \frac{\overline{\text{I}^{\text{all}}_{\text{MCI}}}}{\overline{\text{I}^{\text{patch}}_{\text{MCI}}}} \tag{28}$$

By averaging many $I^{s}_{\text{MCI},j,k}$ values within a patch, we reduce the influence of previously inaccurately compensated AOI and distance effects, reducing the eventual propagation of the estimation errors. Once $\rho'^{\text{mat}_j}_{\varphi_0}$ values are estimated they can be used as known (given) variables in Eqs. (26) and (27). Hence, Cycle 1 can be repeated and $f^{\text{glob}}_{\varphi_0}(\varphi_{j,k})$ and $g^{s}_{R_0}(R_{j,k})$ estimated with a reduced bias due to previously used incorrect assumptions and eventual correlations between the variables. Cycle 2 is repeated until the median change between consecutive iterations for all compensation terms ($f^{\text{glob}}_{\varphi_0}(\varphi_{j,k})$, $g^{s}_{R_0}(R_{j,k})$, and $\rho'^{\text{mat}_j}_{\varphi_0}$) applied to intensity values is below 0.01.

Upon completing the second convergence cycle, $f^{\text{glob}}_{\varphi_0}(\varphi_{j,k})$ and $g^{s}_{R_0}(R_{j,k})$ are used to compensate the raw intensities of the original point clouds using Eq. (22). Using the method presented in this section, it is possible to estimate $I^{s}_{\text{MCI},j,k}$ automatically, in a data-driven way, without conducting additional calibration scans or manual work.

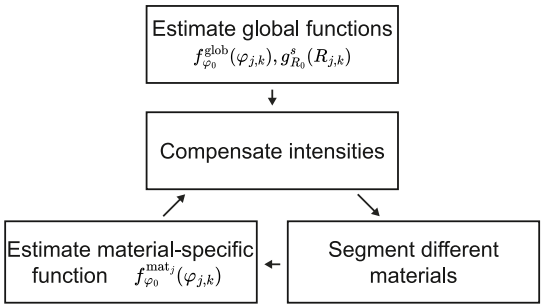

Fig. 3. Expanded method of material dependent radiometric calibration.

3.2. Expansion to material specific compensation

The expansion of the described global compensation method simply substitutes the previously introduced $f^{\text{glob}}_{\varphi_0}(\varphi_{j,k})$ with a set of material specific terms $f^{\text{mat}_j}_{\varphi_0}(\varphi_{j,k})$. Given the distinctive reflectance patterns of different materials, it is assumed that employing material specific $f^{\text{mat}_j}_{\varphi_0}(\varphi_{j,k})$ can significantly improve the quality of modeling and accounting for the effects of the measurement configuration on the intensity values. This change has several consequences for the method's implementation. First, Cycle 1 has to be adjusted to accommodate the simultaneous estimation of several different $f^{\text{mat}_j}_{\varphi_0}(\varphi_{j,k})$ functions. Second, normalized reflectance coefficients $\rho'^{\text{mat}_j}_{\varphi_0}$ are this time estimated per material and not per point cloud patch. Third, each measured point j has to be assigned a material specific identifier relating it to a corresponding $f^{\text{mat}_j}_{\varphi_0}(\varphi_{j,k})$. Hence, there is an additional requirement of having semantically segmented point clouds. Where each semantic class corresponds to a different material.

At the time of writing this article, there are no readily available algorithms that can effectively segment different materials within TLS point clouds. Current research efforts in point cloud segmentation mostly focus on segmenting different objects with a coarse level of detail (e.g. entire houses and buildings, cars, and trees) (Xiang et al., 2023; Zhang et al., 2020; Xu et al., 2020) and such algorithms are not capable of finer separation of different object parts made of different materials. Hence, we did not integrate such a semantic segmentation as a part of the proposed method (e.g. within the point cloud processing step, see Fig. 2). Rather, in the current implementation, such per-point semantic labels are all additional input that needs to be provided by the user. As improving point cloud segmentation is a part of the current research efforts and one of the main expected use-cases that could benefit from $I^{s}_{\text{MCI},j,k}$, as a future development, we envision a recursive method that would incorporate both $I^{s}_{\text{MCI},j,k}$ estimation and semantic segmentation within a single pipeline. A sketch of this envisioned workflow is presented in Fig. 3. However, the development of a suitable semantic segmentation algorithm and full implementation of this envisioned method are out of the scope of this work.

Final remark. In this case of introducing multiple material-specific $f^{\text{mat}_j}_{\varphi_0}(\varphi_{j,k})$, the choice of φ_0 has a significant influence on the $I^{s}_{\text{MCI},j,k}$ values and the results of the downstream tasks relying on them, as each material receives its own $\rho^{\text{mat}_j}_{\varphi_0}$, which influences the relative distribution of resulting $I^{s}_{\text{MCI},j,k}$ values related to each material. This stems from the fact that the split of the target dependent variables ρ and Ω of Eq. (7) into material and/or surface dependent constant $\rho^{\text{mat}_j}_{\varphi_0}$ and AOI dependent function $f^{\text{mat}_j}_{\varphi_0}(\varphi_{j,k})$ is ambiguous. In reality, $f^{\text{mat}_j}_{\varphi_0}(\varphi_{j,k})$ inevitably reflects both information about material properties and surface conditions (see Section 2.1). By choosing φ_0 we can influence which of the latter two properties we want to reflect within $\rho^{\text{mat}_j}_{\varphi_0}$. For example, by choosing a small value for φ_0, $\rho^{\text{mat}_j}_{\varphi_0}$ will more reflect the surface conditions information as it will be highly susceptible to eventual specular reflection. On the contrary, if we chose a higher value for φ_0, we can avoid this effect and steer $\rho^{\text{mat}_j}_{\varphi_0}$ to better reflect inner material properties (e.g. color). The choice ultimately depends on the downstream task relying on $I^{s}_{\text{MCI},j,k}$ and the full information about the material can be retrieved only by considering a full range of φ_0 values.

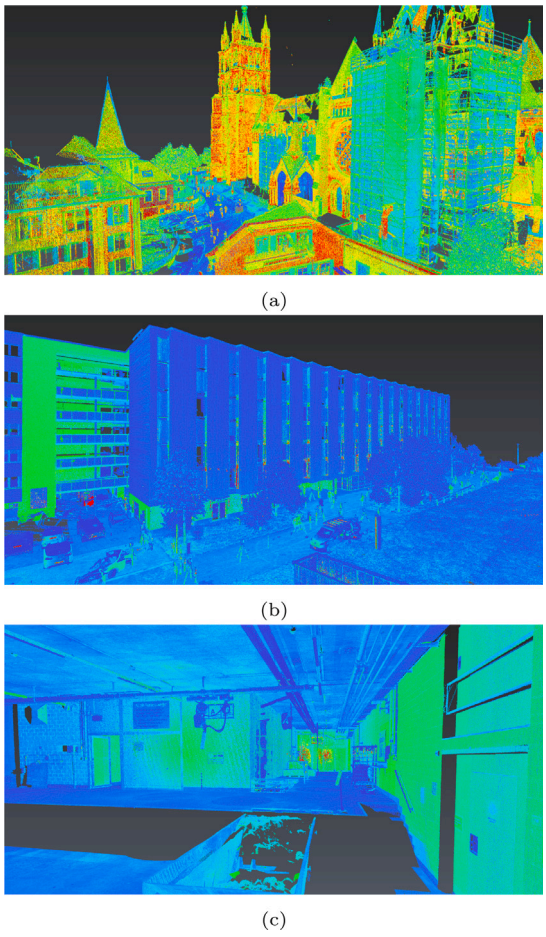

Fig. 4. Point clouds of the acquired datasets colored with the raw intensity: (a) Dataset 1 captured with Z+F Imager 5016, (b) Dataset 2 captured with Leica RTC360, and (c) Dataset 3 also captured with Leica RTC360. (For interpretation of the references to color in this figure legend, the reader is referred to the web version of this article.)

4. Datasets

We collected three datasets (Fig. 4) to evaluate the proposed method, each featuring different measurement configurations, scanned objects and instruments. Table 2 provides an overview of each dataset. The first two datasets were collected outdoors: (a) within a historical district and (b) in a contemporary urban environment. The third dataset (c) was collected indoors in a typical industrial environment. These datasets cover representative objects with varying surface and material properties commonly encountered in practical applications (see Table 2).

We scanned two scenes with more than one TLS and used overall four different instruments with two goals in mind. First, we wanted to investigate the generalizability of the proposed method for different instruments. Second, we wanted to analyze if the radiometrically compensated intensities ($I^{s}_{\text{MCI},j,k}$) of the same objects are more comparable across the instruments than originally recorded "raw" intensities ($I^{s}_{j,k}$), based on the premise that they better represent true material and surface properties. For the latter reason, we selected instruments

Table 2
Overview of captured datasets for the evaluation of the proposed method.
(MSP - median number of different scans covering a patch; Storage - total size of the dataset, including all scans in the file format e57).

Name	Scanners	# scans	# points [10^6]	MSP	Storage	Typical objects/materials
Dataset 1	Z+F Imager 5016	33	756	6	20.8 GB	Cathedral with sandstone facade, street, buildings with stucco facades, trees, people, cars
Dataset 2	Z+F Imager 5016	33	918	15	32.1 GB	Building with plaster and wooden facades, cars, trees, meadow
	Leica RTC360	32	1999	19	55.8 GB	
Dataset 3	Z+F Imager 5016	14	465	5	13.2 GB	Brick and concrete walls, industrial floor, metal surfaces
	Leica RTC360	15	474	6	13.1 GB	
	FARO Focus3D X330 (1)	11	114	4	2.6 GB	
	FARO Focus3D X330 (2)	11	115	4	2.6 GB	

Table 3
Overview of the used scanner settings.

Scanner	FoV	Scanning time [mm:ss]	Resolution	Quality	Registration software
Z+F Imager 5016	Diverse	03:07	High (6.3 mm @ 10 m)	Normal	Z+F Lasercontrol Scout
Leica RTC360	Full	01:42	High (1.9 mm @ 10 m)	–	Leica Cyclone Register 360
Faro Focus 3D X330	Full	01:03	1/8 (12.3mm @ 10 m)	2x	Faro Scene

(see Table 2) operating at the same wavelength, ensuring a consistent expected reflectance of the scanned materials.

We scanned the scenes with approximately 5 m distances between the stations for the outdoor and with 3 m for the indoor datasets. This represents a relatively dense scan distribution compared to typical scanning projects. Similar densities may be used in projects that require capturing all the details of the facades or scene, whereas lower densities are sufficient for projects that only require a rough representation of the environment. However, there is a tendency towards such densification with the increased adoption of cloud-to-cloud based scan registration pipelines, making our datasets reasonably representative of typical use cases. Otherwise, the scanning procedure and scan station selection mostly followed common practices.

Maybe the main exception was that, before the data collection, we performed a warm-up routine with each instrument to mitigate any effects of the internal instrument temperature changes on the measured intensities as shown in Laasch et al. (2023). The warm-up routine consisted of repeated scanning for 1 h from one scanner station and these scans were discarded from further processing. Related, the data acquisition in each case was done within a relatively short time window (<2.5 h) to ensure stable meteorological conditions, minimizing the impact of atmospheric changes on the measured intensities. These measures were primarily taken as precaution due to some literature evidence of the impact of the abovementioned adverse effects on data quality (Janßen et al., 2021). However, they are not a mandatory requirement for a successful application of the proposed method.

The point clouds captured with individual instruments were co-registered (aligned) within a common local coordinate system using the manufacturer's proprietary registration software (see Table 3), employing the established cloud-to-cloud (targetless) registration algorithms as part of the standard data processing pipelines. Afterwards, the point clouds of one scene captured with different instruments were co-registered as well to establish direct spatial correspondences. This co-registration was performed using the ICP algorithm implemented in CloudCompare, following a manual coarse alignment.

The resulting point clouds were exported with corresponding intensity values, which are subjected to the undisclosed preprocessing procedures within the manufacturer's proprietary software. The resulting values are likely somewhere in between $I^s_{j,k}$ and $I^s_{\mathrm{MCI},j,k}$ values, where the level up to which the radiometric compensation was applied is unknown. The only exception was the case of the Z+F Imager 5016 scanner data. The Z+F Imager 5016 intensities can be and were exported both as raw not-preprocessed values (as recorded by the instrument's APD and then digitized; $I^s_{j,k}$) and as "reflectance values". In this case, from the personal correspondence with the manufacturer we know that the "reflectance values" refer to the raw intensity values $I^s_{j,k}$ compensated for the range dependent effects ($g^s_{R_0}(R_{j,k})$) and instrument dependent factor ($\kappa^s_{R_0}$), empirically determined by the manufacturer during the factory-based calibration using a radiometric reference target with 80% reflectance. Hence, these values do not represent true reflectance but an approximation, as they do not account for influences related to the second term in Eq. (4) (AOI, material and surface related properties encapsulated within $f^{\mathrm{mat}_j}_{\varphi_0}(\varphi_{j,k})$). Finally, the point clouds (with intensities), expressed in a common coordinate system for each dataset and accompanied by pose information for each scanner position (transformation parameters between scan-centric and common local CS) were used as input for the $I^s_{\mathrm{MCI},j,k}$ computation method presented in the previous section. For these computations, we used a computer with 64 GB RAM (without using a GPU).

5. Results

This section focuses on our method for global radiometric compensation (Section 3.1) and retrieving $I^s_{\mathrm{MCI},j,k}$ values, but also presents a demo of the expanded workflow for material-specific compensation (Section 3.2). We compare our global compensation method with the related state of the art (Section 5.1) and test its generalizability (Section 5.4). In a meta-analysis (Sections 5.2 and 5.3), we further show how the choice of the functional model for $f^{\mathrm{mat}_j}_{\varphi_0}(\varphi_{j,k})$ impacts the performance, and compare the results of fully on-site vs. combined compensation, which is possible in the case of previously determined and available parameters $g^s_{R_0}(R_{j,k})$ and $\kappa^s_{R_0}$. Finally, we demonstrate how we can benefit from the retrieved $I^s_{\mathrm{MCI},j,k}$ for: (i) point cloud segmentation (Section 5.6); (ii) material probing (Section 5.5); (iii) integrating data acquired using different TLS instruments (Section 5.7).

5.1. Comparison to state-of-the-art methods

To test the performance of our global radiometric compensation, we compare it with three state-of-the-art comparable methods introduced in the following works: Carrea et al. (2016), Li et al. (2023) and Tan et al. (2020). The chosen methods are the instances of combined compensation (Section 2.2), combining lab and on-site measurements and requiring partially manual processing, while our method is primarily

designed as fully on-site method capable of automatic simultaneous estimation of $f_{\varphi_0}^{\text{mat}_j}(\varphi_{j,k})$ and $g_{R_0}^{s}(R_{j,k})$. This choice was made as no other method provides the possibility for complete on-site compensation. In Carrea et al. (2016) and Li et al. (2023) the intensities are compensated for the range-related effect based on $g_{R_0}^{s}(R_{j,k})$ determined through previous lab experiments, while the AOI-related effect is accounted for using in-situ estimated $f_{\varphi_0}^{\text{mat}_j}(\varphi_{j,k})$. In Tan et al. (2020) the case is the opposite.

Carrea et al. (2016) focused on long-range scans, demonstrating in lab experiments that the range dependent system transmission $\eta_R^s(R)$ (see Eq. (3)) is constant for distances over 100 m for the Optech ILRIS-3D$^{\text{ER}}$ and Optech ILRIS-LR. Therefore, they compensate the intensities for the remaining distance-related effect simply by modeling $g_{R_0}^{s}(R_{j,k})$ as $\frac{1}{R^2}$. For compensating the AOI effect, their method relies on visually identifying and manually segmenting larger surfaces with homogeneous material and surface properties and estimates $f_{\varphi_0}^{\text{mat}_j}(\varphi_{j,k})$ per segmented surface. They use the distribution of intensity vs. AOI value point pairs for optimization, originating from either one or multiple scans without explicitly benefiting from scan overlaps. They chose the Oren–Nayar model (Oren and Nayar, 1994) as a functional model for $f_{\varphi_0}^{\text{mat}_j}(\varphi_{j,k})$ because they work with rock surfaces that are primarily diffuse. This model uses one parameter, which represents the surface roughness.

Because our data consists of short-range scans with measured ranges of less than 100 m, we can no longer assume the constant system transmission η_{Sys}. Therefore, to allow for a fair comparison, we performed measurements in the lab using a Lambertian target with 80% reflectance (Spectralon®) to estimate $g_{R_0}^{s}(R_{j,k})$. The function is approximated with smoothing splines fitted to 2D data points consisting of measured intensity values and known ranges for the target placed at 20 cm intervals from 1.4 m to 50 m. Additionally, we defined manually homogeneous areas for the in-situ estimation of $f_{\varphi_0}^{\text{mat}_j}(\varphi_{j,k})$, as Carrea et al. (2016).

In Li et al. (2023), the authors use a piece-wise approximation of $g_{R_0}^{s}(R_{j,k})$, using a higher-order polynomial for the near-range effect $\eta_R^s(R)$ and an exponential function for the exponential decay of the signal $\frac{1}{R^2}$ (see Eq. (12)). The function parameters are determined based on the same lab experiments as described in the previous paragraph. For the AOI compensation, similarly to Carrea et al. (2016) and Li et al. (2023) manually select areas with assumed uniform reflectance to fit the Blinn–Phong model (Blinn, 1977) and correct the already distance-compensated intensity for the AOI effect.

Tan et al. (2020) estimate $f_{\varphi_0}^{\text{mat}_j}(\varphi_{j,k})$ by fitting a 3rd-order polynomial to the lab data, which was obtained by measuring four Lambertian targets with different reflectance scanned with an AOI ranging from 0° to 85° in 5° steps. To compensate the already AOI-compensated intensities for the distance effect, they measured a long street segment that they cut out manually and assumed it had uniform reflectance.

To compare our method with the three mentioned ones, we implemented them based on the descriptions in the papers and applied them to our datasets. For the comparison, we manually segmented different large areas (up to a length of 15 m) with consistent backscattering characteristics (e.g. see Fig. 5). Overall, we chose 30 areas across all datasets to represent various materials with different backscattering characteristics. The following list describes which materials are segmented in which dataset (see Section 4):

- **Dataset 1:** house facade, sandstone brick of cathedral, metallic surface
- **Dataset 2:** plaster facade, wooden facade, asphalt, metallic container
- **Dataset 3:** brick wall, wooden door, metallic cabinet, metallic door, painted concrete floor

In the evaluation, we compare the intensities of points measured from different scan stations within one of the abovementioned areas

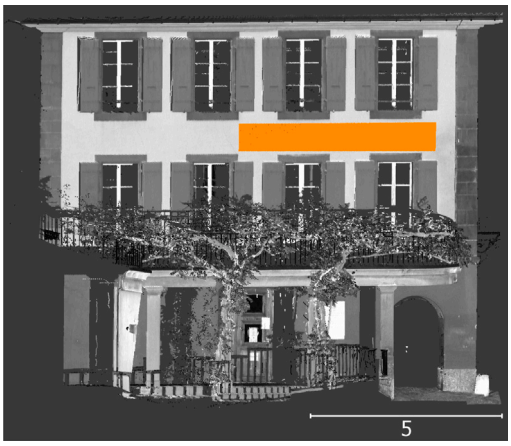

Fig. 5. Defined area (orange part) of a house facade. The point cloud is colored with the $I_{\text{MCI},j,k}^{s}$.
(Dataset 1, Z+F Imager 5016). (For interpretation of the references to color in this figure legend, the reader is referred to the web version of this article.)

($I_{\text{r},j,k}^{s}$ and $I_{\text{MCI},j,k}^{s}$). The areas of Datasets 1 and 2 contain points captured from 10 to 30 stations, and Dataset 3 includes points from 3 to 10 stations. We deliberately choose areas that are covered by a large number of (not necessarily overlapping) scans to ensure robust statistical quantities (metrics) that we use in the following evaluation.

Fig. 6 shows one example of histograms once for the raw intensities $I_{\text{r},j,k}^{s}$ (see Fig. 6(a)) and once for the $I_{\text{MCI},j,k}^{s}$ (see Fig. 6(b)) of the points lying in the defined area in Dataset 1 shown in Fig. 5. Each color represents a scan station captured with different AOI and distance to the area. Only six different scan stations are shown in the histogram because the ones far away have much fewer points inside this area and are therefore mitigated. As we see in Fig. 6(a), the distributions of the raw intensities of the different scan stations are notably different due to the influences of the measurement configuration, which can be observed by (a) noticeable mean shifts and (b) wide spread of values. In the ideal case of no bias, no measurement noise, and an entirely uniform surface, all intensities should be represented by a single scalar value.

After the radiometric compensation and computing the $I_{\text{MCI},j,k}^{s}$ values using the proposed method with the AL+SS AOI model (best performing AOI model, see Section 5.2), both the bias between the point clouds and the overall spread intensities decrease (as depicted in Fig. 6(b)). This indicates that the compensation successfully reduces the measurement configuration impact on intensities.

To describe the latter behavior of the intensity values quantitatively and to be able to compare the performance of different methods, we use (and define) four separate metrics:

- **Bias**: We selected the bias metric, defined as the median absolute deviation (MAD) of the medians of the intensities for each individual point cloud divided by the median of all intensities, because it represents the offset of the intensities between the scan stations. Our main objective is to minimize this offset, ensuring the scan stations align consistently.
- **Internal spread**: The internal spread, calculated as the median of the MADs of the intensities in each individual point cloud divided by the median of all intensities, was chosen to control the noise of the intensities and the small systematic variations in the intensities due to the measurement configuration within one point cloud. By focusing on individual point clouds, this metric helps us assess the level of internal variation. It ensures that the systematic variation due to the measurement configuration is reduced and the noise is not increased. This metric often provides

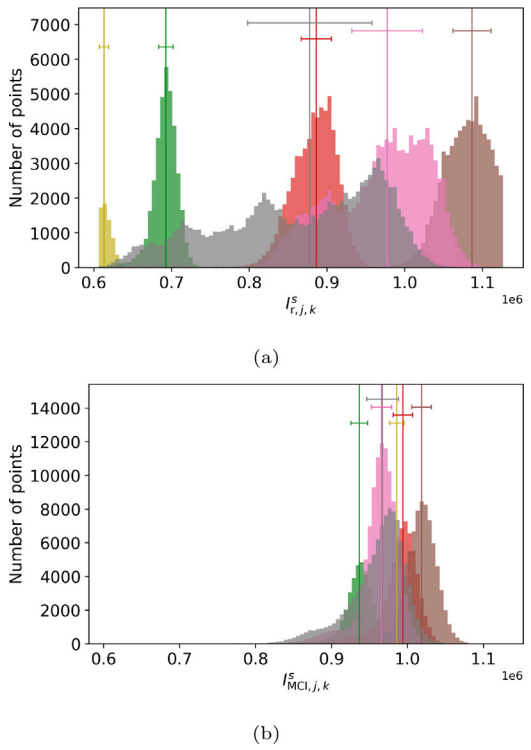

Fig. 6. Histogram with raw intensities $I^s_{r,j,k}$ (a) and $I^s_{MCI,j,k}$ (b) for the area shown in Fig. 5. Different colors represent different point clouds captured with different measurement configurations. The vertical lines show the median value of each point cloud and the horizontal lines the corresponding MAD.
(Dataset 1, Z+F Imager 5016). (For interpretation of the references to color in this figure legend, the reader is referred to the web version of this article.)

much information about the noise level because the systematic variations are often very small due to similar distance and AOI values.

- **Overall spread**: The overall spread, defined as the MAD of all intensities of all point clouds divided by the median of all intensities, combines the effects of bias and internal spread. We aim to minimize the overall spread as it encapsulates the variability of the entire dataset.
- **Coefficient of Variation (CV)**: The CV, defined as the standard deviation divided by the mean of all intensities, is a commonly used and widely understood metric. We included CV because it provides a normalized measure of variability that is easy to interpret and compare across datasets and methods. Instead of the other metrics, this metric is not robust and shows us the influence of outliers compared with the others.

The metrics are calculated for each inspected area and averaged over all areas related to one dataset and scanner. The division in each metric by the mean or median of all intensities is to have scale-invariant metrics.

In addition to these metrics, we also examined correlation matrices between the point clouds as an alternative evaluation approach. Specifically, we computed the mean $I^s_{r,j,k}$ and $I^s_{MCI,j,k}$ for the common patches of both point clouds and calculated their correlation. Generally, we found the correlation coefficients between the $I^s_{MCI,j,k}$ values for the same materials and surface types higher than those between the raw intensities. However, the empirical (co-)variances and correlation coefficients are strongly affected by the grossly varying number of scans per patch and differences in correlation of reflectances, distances, and AOIs, and are thus challenging to interpret quantitatively. Given these complexities, we focus on the metrics derived from the distributions within the areas and leave further investigation of correlation matrices for future work.

Table 4
Comparison of our own method and state-of-the-art methods. Best metrics are shown in bold.
(Dataset 1, Z+F Imager 5016).

Method	Bias	Overall spread	Internal spread	CV
Raw	0.18	0.11	**0.03**	0.21
Carrea et al. (2016)	0.14	0.12	0.04	0.20
Li et al. (2023)	0.26	0.38	0.25	24.28
Tan et al. (2020)	0.67	0.17	0.07	0.57
Own method (ON)	0.16	0.13	0.04	0.20
Own method (AL+SS)	**0.06**	**0.05**	**0.03**	**0.11**

Table 5
Metrics for $I^s_{MCI,j,k}$ computed with different AOI models. Best metrics are shown in bold.
(Dataset 1, Z+F Imager 5016).

AOI model	Bias	Overall spread	Internal spread	CV
Raw	0.18	0.11	**0.03**	0.21
L	0.12	0.07	0.04	0.57
LB	**0.06**	0.07	**0.03**	0.61
LSL	0.07	0.06	0.04	0.63
BP	0.13	0.07	0.04	0.57
ON	0.16	0.13	0.04	0.20
AL	0.07	**0.05**	**0.03**	0.12
SS	**0.06**	0.06	**0.03**	0.12
AL+SS	**0.06**	**0.05**	**0.03**	**0.11**

Table 4 presents the metrics for the raw intensity and the $I^s_{MCI,j,k}$ computed with the state-of-the-art methods and our method with different AOI models. Our method (with AL+SS) generally outperforms the others, making the intensities more uniform without increasing the noise. Part of this success comes from the generalizability of our method through the flexible choice of the functional model for $f^{mat_j}_{\varphi_0}(\varphi_{j,k})$. If we are choosing, for example, the ON model, the same model as Carrea et al. (2016) are using, we get similar metric values compared to the Carrea et al. (2016) method. However, the bias and overall spread are slightly worse because we are estimating just one global function for the whole dataset, and Carrea et al. (2016) calculate a function for the points of each point cloud inside each area. Hence, our method with AL+SS gets better metric values and works automatically instead of the state-of-the-art methods.

5.2. Comparison of AOI models

As seen before, the choice of the AOI model has a notable impact on the results of radiometric compensation. As this work aims to provide a radiometric compensation method that generalizes well across different datasets, we tested several AOI models (see Table 1) in search of the most generalizable one. Table 5 shows the metrics of the raw intensities and the $I^s_{MCI,j,k}$ computed with each AOI model for Dataset 1 acquired with Z+F Imager 5016 (the results calculated based on other datasets are comparable). The metrics indicate that irrespective of the AOI model choice, our method reduces the measurement configuration impact on intensities. The internal spread increases slightly with some of the AOI models because of higher noise in the $I^s_{MCI,j,k}$, due to the additional uncertainty of the AOI estimation, or not perfectly fitted $f^{glob}_{\varphi_0}(\varphi_{j,k})$ and $g^s_{R_0}(R_{j,k})$, so systematic variations arise due to local erroneous compensated measurement configuration effect.

The models introduced in this study (AL, SS, and AL+SS) perform best and are comparable across all metrics, where AL+SS is marginally better. An additional reason for choosing AL+SS instead of, e.g., a much simpler and more robust AL model is that the flexibility of the smoothing spline is expected to have even higher relevance in the case of estimating the material-specific $f^{glob}_{\varphi_0}(\varphi_{j,k})$, which could get notably different from AL in cases of modeling the behavior of highly

Table 6
Comparison of the metrics of the raw intensity, the compensated intensity with estimated distance and AOI, the reflectance values compensated with AOI and once with AOI and distance. Best metrics are shown in bold.
(Dataset 1, Z+F Imager 5016, AL+SS AOI model).

Data	Compensation	Bias	Overall spread	Internal spread	CV
Intens.	None	0.18	0.11	0.03	0.21
Intens.	AOI & Dist.	0.06	**0.05**	0.03	0.11
Reflect.	AOI	**0.05**	0.07	0.03	0.11
Reflect.	AOI & Dist.	0.07	**0.05**	0.03	**0.10**

specular materials. Instead of using SS, the AL+SS is much more robust regarding the correlation of the distance and AOI due to the first approximation with the AL model. Hence, if not otherwise stated, we use the AL+SS model for the following analysis.

5.3. On site vs. combined compensation

As demonstrated in Section 5.1, the proposed method allows for automatic on-site estimation of both $f^{\text{glob}}_{\varphi_0}(\varphi_{j,k})$ and $g^{s}_{R_0}(R_{j,k})$ functions. However, in some cases, the users could have available priors, for example, $g^{s}_{R_0}(R_{j,k})$, estimated during the factory calibration. This allows us to use our method as combined compensation and estimate only $f^{\text{glob}}_{\varphi_0}(\varphi_{j,k})$ on site. In this section, we wanted to investigate if such an approach improves the quality of the derived $I^{s}_{\text{MCI},j,k}$ values.

As described in Section 4, it is possible to export the reflectance values (intensities compensated for $g^{s}_{R_0}(R_{j,k})$ and $\kappa^{s}_{R_0}$) for the Z+F Imager 5016. Therefore, for this analysis, we used the raw intensities and the reflectances of Dataset 1 as an example because the overlap of the scan stations is high (see Section 4). For the compensation, we can estimate the $f^{\text{glob}}_{\varphi_0}(\varphi_{j,k})$ and $g^{s}_{R_0}(R_{j,k})$ once for the raw intensities and once for the reflectances. Additionally, we can estimate only $f^{\text{glob}}_{\varphi_0}(\varphi_{j,k})$ by fixing $g^{s}_{R_0}(R_{j,k})$ constant at 1 for the reflectances because they are already distance compensated.

The results are presented visually in Fig. 7 and numerically in Table 6. Fig. 7 presents the three cases of estimating $f^{\text{glob}}_{\varphi_0}(\varphi_{j,k})$ and $g^{s}_{R_0}(R_{j,k})$. We expect that in the case of reflectances, the estimated $g^{s}_{R_0}(R_{j,k})$ is a straight line (see Fig. 7(a)). However, there is still a trend in the distance dependence $g^{s}_{R_0}(R_{j,k})$. This trend can likely occur due to coupling of the correlated variables (e.g., distance with reflectance) or imperfect AOI compensation, resulting in biased $f^{\text{glob}}_{\varphi_0}(\varphi_{j,k})$ estimates.

Fig. 7(b) shows that the estimated functions for the reflectance are significantly different once estimating $f^{\text{glob}}_{\varphi_0}(\varphi_{j,k})$ and $g^{s}_{R_0}(R_{j,k})$ and once only $f^{\text{glob}}_{\varphi_0}(\varphi_{j,k})$, as the estimated standard deviations of $\pm 3\sigma$ are not overlapping. The empirical standard deviation is estimated using an adapted bootstrapping algorithm (Efron, 1982), which estimates the compensation functions 100 times using 20% of the neighborhood patches. The difference of $f^{\text{glob}}_{\varphi_0}(\varphi_{j,k})$ indicates that when estimating both $f^{\text{glob}_j}_{\varphi_0}(\varphi_{j,k})$ and $g^{s}_{R_0}(R_{j,k})$, we are likely compensating a part of the AOI effect with $g^{s}_{R_0}(R_{j,k})$ due to the high correlation. Both AOI functions $f^{\text{glob}}_{\varphi_0}(\varphi_{j,k})$ of the estimation with the raw intensities and reflectance (AOI & Distance) are similar. Therefore, $g^{s}_{R_0}(R_{j,k})$ of the raw intensity contains very likely the same trend as in the estimated $g^{s}_{R_0}(R_{j,k})$ of the reflectances.

Table 6 shows the metrics of the not compensated raw intensity and the three abovementioned cases. There, we see that the bias is smaller when using the reflectances and estimating only $f^{\text{glob}}_{\varphi_0}(\varphi_{j,k})$, but the overall spread and CV are lower when $f^{\text{glob}}_{\varphi_0}(\varphi_{j,k})$ and $g^{s}_{R_0}(R_{j,k})$ are estimated with reflectances or intensities. The results show that solutions with or without adding priors are generally comparable. Hence, adding priors does not necessarily lead to better $I^{s}_{\text{MCI},j,k}$ estimates. However, we recommend including them as a precaution against overfitting in the case of reduced data quality and/or quantity.

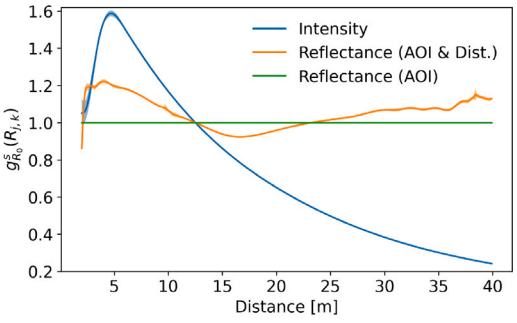

(a)

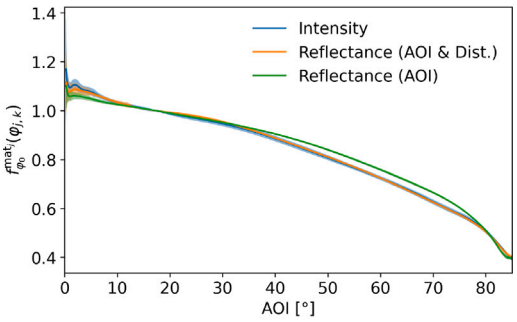

(b)

Fig. 7. Fitted distance (a) and AL+SS AOI (b) functions with three times the standard deviation for the raw intensities and the reflectance values. For the reflectance values we distinguish between two cases, where once the distance compensation is fixed to 1 and once is also estimated.
(Dataset 1, Z+F Imager 5016, AL+SS AOI model).

Table 7
Comparison of the three datasets. Best metrics are shown in bold.
(Z+F Imager 5016).

Dataset	AOI model	Bias	Overall spread	Internal spread	CV
1	Raw	0.18	0.11	**0.03**	0.21
	AL+SS	**0.06**	**0.05**	**0.03**	**0.11**
2	Raw	0.14	0.21	0.04	0.33
	AL+SS	0.11	0.09	0.07	0.20
3	Raw	0.32	0.12	**0.03**	0.38
	AL+SS	0.20	0.06	0.04	0.38

5.4. Generalizability

In this subsection, we analyze the generalizability of our method across different datasets and scanners and the transferability of estimated $f^{glob}_{\varphi_0}(\varphi_{j,k})$ and $g^{s}_{R_0}(R_{j,k})$ across datasets.

Generalizability of the method: As part of the generalizability analysis, we test the method's generalizability across different datasets. For the evaluation, we computed the previously introduced metrics (see Table 7) for each dataset using the Z+F Imager 5016, as it is the only instrument used in all three datasets.

In Table 7, we can observe that by applying the compensation, the overall spread, the bias, and the CV decrease for each dataset. This decrease in the metrics shows that our method is generalizable across different datasets. However, the internal spread increases slightly with the datasets 2 and 3 due to higher noise and/or higher systematic variations, as described in Section 5.2. Since our primary goal is to reduce the bias between the point clouds and to calculate the internal spread solely to control noise and systematic variations within a point cloud, this slight increase is not a major concern, as it remains smaller than the bias.

Table 8 shows the metrics of each scanner for dataset 3 to evaluate the generalizability across different instruments. Each scanner has a

Table 8
Percental change of the metric with respect to the metric for the raw intensity for different scanners. Best metrics are shown in bold.
(Dataset 3, AL+SS AOI model).

Scanner	Bias change	Overall spread change	Internal spread change	CV change
Z+F Imager 5016	−0.38	−0.50	0.18	−0.01
Leica RTC360	**−0.55**	−0.32	**−0.10**	−0.40
Faro Focus3DX330 (1)	−0.52	−0.44	0.01	−0.32
Faro Focus3D X330 (2)	−0.48	**−0.53**	0.10	**−0.47**

distinct definition of intensity, resulting in different intensity ranges. To mitigate these influences, we represent the values as percentage changes with respect to the metric of the raw intensities. All metrics, except the internal spread, are improved with radiometric calibration, indicating that the compensation increases the independence of intensities from measurement configuration factors for all instruments.

Generalizability of the estimated functions: In the previous analysis, we proved that the method is applicable across datasets and instruments. Here, we investigate if the estimated compensation functions $f_{\varphi_0}^{\text{glob}}(\varphi_{j,k})$ and $g_{R_0}^{s}(R_{j,k})$ are generalizable and, therefore, transferable across different datasets. Hence, we want to answer the question: Can we estimate the globally optimal $f_{\varphi_0}^{\text{glob}}(\varphi_{j,k})$ and $g_{R_0}^{s}(R_{j,k})$ once for a given instrument and then use them for multiple datasets? For this reason, we analyze how similar the compensation functions are across the datasets. Fig. 8 shows the compensation functions for the three datasets captured with the Z+F Imager 5016 and the empirical standard deviation calculated with the abovementioned adapted bootstrapping algorithm.

Fig. 8(a) indicates that the estimated AOI functions $f_{\varphi_0}^{\text{glob}}(\varphi_{j,k})$ differ significantly. This is likely because the scenes have different predominant materials and surface conditions, such as diffuse, specular, or rough surfaces. For example, we have increased $f_{\varphi_0}^{\text{glob}}(\varphi_{j,k})$ values at low incidence angles in the Dataset 3 because of the predominantly specular materials (Bai et al., 2024). Therefore, it is better to estimate the AOI function for each dataset individually.

Together with the AOI functions, the distance functions $g_{R_0}^{s}(R_{j,k})$ are also significantly different between the datasets (see Fig. 8(b)). As described in Section 2.1, $g_{R_0}^{s}(R_{j,k})$ only depends on the system transmission $\eta_{R_0}^{s}(R)$ and the $1/R^2$ factor (see Eq. (12)). That means that irrespective of the scene, the distance dependence should be equal between the scenes. Our result seems to contradict. First, as mentioned in Section 5.3, the AOI function $f_{\varphi_0}^{\text{glob}}(\varphi_{j,k})$ can influence the distance function because the data are highly correlated. Second, a part of the reflectances is absorbed by the distance function because they are not uniformly distributed over the distances.

The observable large deviation of $g_{R_0}^{s}(R_{j,k})$ of Dataset 3 relative to the others is likely due to the non-uniform distribution of materials with high specular reflectance in the indoor case, which biases the estimation process. For example, in Fig. 8(b), we see that the distance dependence of Dataset 3 has some unexpected artifacts (peaks and troughs) around 10 to 15 m. Based on the visual inspection of the dataset, we assume that these artifacts come from highly reflective objects clustered at these distances.

To assess the negative impact of these artifacts on the quality of the estimated $I_{\text{MCI},j,k}^{s}$, we calculated the metrics for Dataset 3 using two different distance functions $g_{R_0}^{s}(R_{j,k})$: one estimated with Dataset 3 and one estimated with Dataset 1 (see Table 9). Dataset 1 contains more data, has a higher distribution of AOIs and distances within each patch, and includes more diffuse materials. This likely results in a distance function $g_{R_0}^{s}(R_{j,k})$ better representing the actual behavior. The impact of the number of patches, the number of scans covering the individual patches, and the differences of AOIs and distances per patch on the quality of the results has not been analyzed and is left for future work.

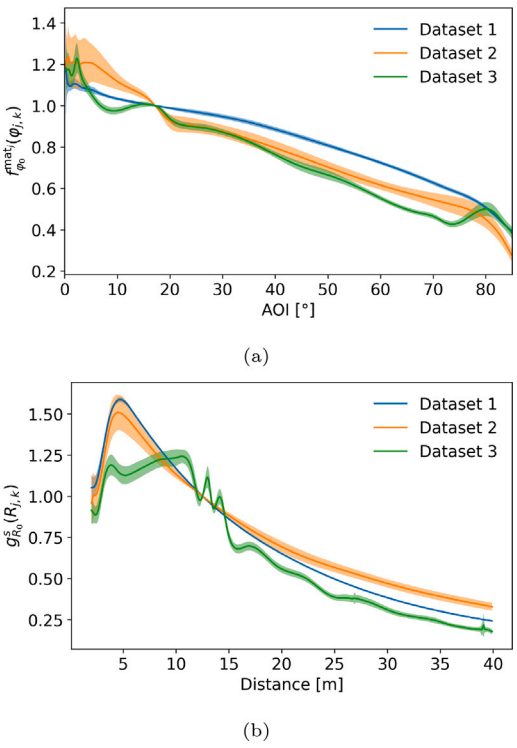

Fig. 8. Fitted AL+SS AOI (a) and distance (b) functions with three times the standard deviation for the raw intensities of three datasets.
(Z+F Imager 5016, AL+SS AOI model).

Table 9
Comparison of the metrics of Dataset 3 with the estimated distance function $g_{R_0}^{s}(R_{j,k})$ of Datasets 1 and 3. Best metrics are shown in bold.
(Dataset 3, Z+F Imager 5016, AL+SS AOI model).

Dataset of estimated functions	Bias	Overall spread	Internal spread	CV
Raw	0.32	0.12	**0.03**	**0.38**
3	**0.20**	**0.06**	0.04	**0.38**
1	0.26	0.07	**0.03**	0.39

The values indicate that the estimation of $I_{\text{MCI},j,k}^{s}$ calculated with the same dataset is still better even if we have artifacts because of correlated data. That means the combination of the AOI and distance functions $f_{\varphi_0}^{\text{glob}}(\varphi_{j,k})$ and $g_{R_0}^{s}(R_{j,k})$ are optimized for the specific dataset. Despite overfitting, we could still get $I_{\text{MCI},j,k}^{s}$ that are more useful than raw intensities $I_{\text{r},j,k}^{s}$ for downstream tasks.

Two main conclusions can be drawn from the analysis in this section: (1) our method generalizes effectively across various datasets and scanners; (2) as expected from the theory, a non-in-situ distance function $g_{R_0}^{s}(R_{j,k})$ results in better performance; however, our experimental results show no striking advantage.

5.5. Expanded method and its benefit for material probing

This subsection demonstrates how the extended workflow incorporating material-specific $f_{\varphi_0}^{\text{mat}_j}(\varphi_{j,k})$ (see Section 3.2) can enhance the precision of $I_{\text{MCI},j,k}^{s}$ and material probing. With a material-segmented point cloud, we estimate an individual AOI function for each material $f_{\varphi_0}^{\text{mat}_j}(\varphi_{j,k})$ and one distance function $g_{R_0}^{s}(R_{j,k})$ for the whole point cloud. That enables us to model backscattering characteristics of each material independently and to compensate the $I_{\text{r},j,k}^{s}$ individually for specular, diffuse, or surface roughness properties. The material-specific AOI compensation should lead to more precise $I_{\text{MCI},j,k}^{s}$ and give us

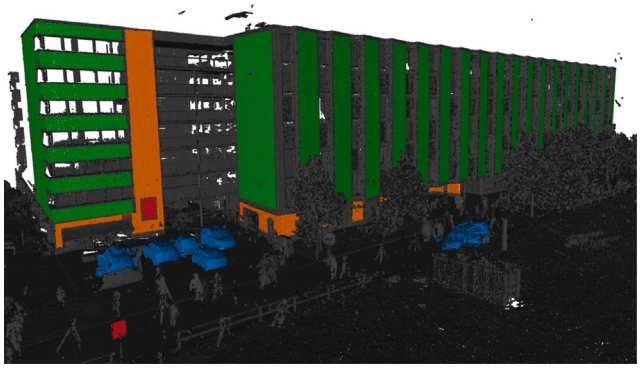

Fig. 9. Manual classification with the following classes: orange: plaster facades, green: wooden facades, blue: cars, red: other metallic surfaces.
(Dataset 2, Leica RTC360). (For interpretation of the references to color in this figure legend, the reader is referred to the web version of this article.)

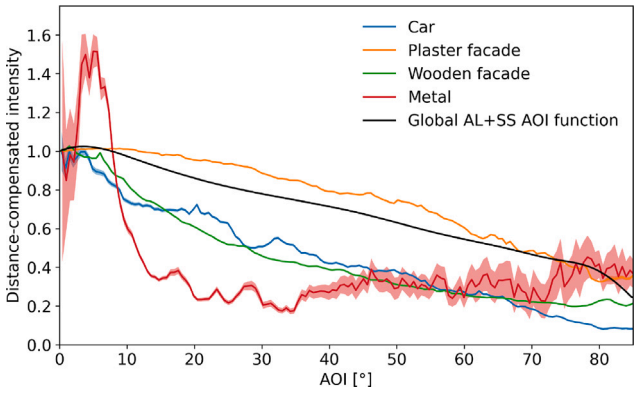

Fig. 10. Distance compensated intensities for each class in dependence of the AOI effect (color coding as in Fig. 9). The patch around the line shows three standard deviations of the averaged intensities for each bin. The global compensation function is the estimated AL+SS AOI model for the entire dataset.
(Dataset 2, Z+F Imager 5016). (For interpretation of the references to color in this figure legend, the reader is referred to the web version of this article.)

additional information about the reflectance properties of each single material segment.

In order to facilitate material-specific AOI function $f_{\varphi_0}^{\mathrm{mat}_j}(\varphi_{j,k})$ estimation, it is essential to have a point cloud segmented according to different materials. Given the absence of suitable algorithms, we manually segmented Dataset 2, which features several larger objects (surfaces) with consistent yet distinctly different material properties (see Fig. 9). We segmented four classes: plaster facade, wooden facade, cars, and other metallic surfaces (not corresponding to cars). The facade classes were chosen because they contain many points with different R and φ values and ensure the assumption of consistent characteristics. The classes related to cars and other metallic surfaces were selected due to their anticipated high specular reflection. Hence, we expect behavior that is noticeably different from that of the facade classes. They were subdivided into two subclasses to examine the similarity in their reflection patterns.

By relying on the manual classification and the previously estimated global distance function $g_{R_0}^s(R_{j,k})$, we can compute the distance-compensated intensities for each class and investigate how these intensities are distributed across AOI, as depicted in Fig. 10. As can be seen based on the range of expectation for most data points (defined by the mean ±3 standard deviations), all curves are significantly different from each other and also significantly different from the global estimated AOI function $f_{\varphi_0}^{\mathrm{glob}}(\varphi_{j,k})$. This indicates that we can improve the precision of $I_{\mathrm{MCI},j,k}^s$ by estimating separate AOI functions for each class of material instead of a global AOI function $f_{\varphi_0}^{\mathrm{glob}}(\varphi_{j,k})$. We tested this by applying our expanded method to the subselected data presented in Fig. 9, estimating material dependent $f_{\varphi_0}^{\mathrm{mat}_j}(\varphi_{j,k})$ for each of the four classes, and subsequently computing the $I_{\mathrm{MCI},j,k}^s$ values.

Table 10 presents the evaluation metrics for the success of the radiometric compensation (as described in Section 5.1) after the (local) material-specific AOI and global distance compensation, $f_{\varphi_0}^{\mathrm{mat}_j}(\varphi_{j,k})$ and $g_{R_0}^s(R_{j,k})$, for all classes compared to the metrics of the raw intensities and the global compensated $I_{\mathrm{MCI},j,k}^s$. The results are presented for each class separately. Instead of the facade classes, the car and metal classes do not show a decrease in all metrics. We assume that this is (a) because the classes are more inhomogeneous, due to different physical material properties within the same class (introducing offsets between the values even if they exhibit similar dependency to AOIs); (b) because there are fewer points in the classes; and (c) there is a potential for multipath effects due to strong reflections that could influence the recorded intensities. However, we see that we can improve the $I_{\mathrm{MCI},j,k}^s$ estimates for the facade classes that are guaranteed to be more homogeneous and are not prone to systematic errors due to specular reflection. That confirms that the material-specific extension of our method can help

Table 10
Comparison of the global and local material-specific AOI compensations. Best metrics are shown in bold.
(Dataset 2, Z+F Imager 5016).

	Compensation	Bias	Overall spread	Internal spread	CV
Plaster facade	Raw	0.26	0.34	0.08	0.39
	Global	0.12	0.11	0.07	0.17
	Local	**0.03**	**0.04**	**0.03**	**0.12**
Wooden facade	Raw	0.11	0.42	0.40	0.72
	Global	0.13	0.21	0.22	0.48
	Local	**0.03**	0.18	0.18	0.45
Car	Raw	0.18	0.96	0.11	1.12
	Global	0.24	0.95	0.34	1.02
	Local	0.28	0.88	0.40	1.00
Metal	Raw	0.30	0.66	0.27	1.41
	Global	1.07	0.53	0.89	1.10
	Local	0.61	0.42	0.65	1.11

to better account for measurement configuration effect on the intensity values.

Moreover, different shapes of the curves presented in Fig. 10 correspond to different material (backscattering) characteristics. For instance, the visible peak in intensity values at low AOI for metal surfaces indicates specular reflection, distinguishing it from other material classes. In contrast, the higher intensity values observed at larger AOIs for plaster facades are likely due to higher surface roughness, which is also unique to this material. Hence, a simple visual inspection of Fig. 10 demonstrates that estimating the material dependent $f_{\varphi_0}^{\mathrm{mat}_j}(\varphi_{j,k})$ and evaluating it at specific AOI values can support material probing tasks. When combined with a database of known values, this approach can serve as a valuable tool for enhancing the semantic interpretation of point clouds.

5.6. Benefit for segmentation tasks

This subsection exemplarily shows how point cloud segmentation can benefit from the $I_{\mathrm{MCI},j,k}^s$ values. To give a simple demonstration, we used the RGB region growing algorithm (Zhan et al., 2009) to segment a point cloud, where we introduced the $I_{\mathrm{MCI},j,k}^s$ values by transforming them into RGB values based on the HUE colormap. For this demonstration, we chose one section of Dataset 1 and one of Dataset 2, where we segmented each section once using the raw intensity $I_{r,j,k}^s$ and once using the $I_{\mathrm{MCI},j,k}^s$ values. In Fig. 11, we present the results of the segmentation. It is evident that the segmentation using $I_{\mathrm{MCI},j,k}^s$

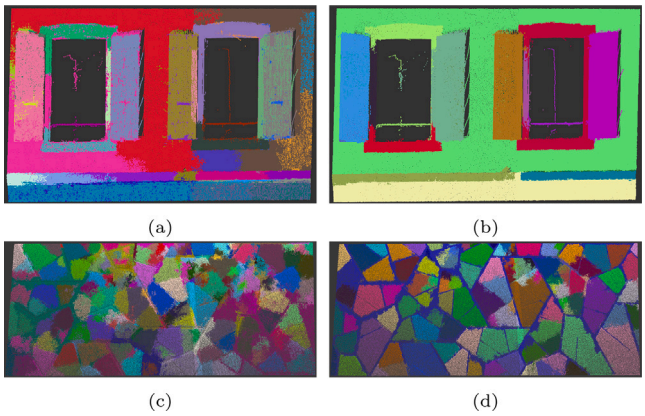

Fig. 11. RGB region growing with the raw intensities $I^s_{r,j,k}$ and $I^s_{\mathrm{MCI},j,k}$ as RGB values transformed with the HUE colormap performed with sections of dataset 1 and 2: window facade with (a) $I^s_{r,j,k}$ and with (b) $I^s_{\mathrm{MCI},j,k}$, tiled floor with (c) $I^s_{r,j,k}$ and with (d) $I^s_{\mathrm{MCI},j,k}$.
(Z+F Imager 5016, AL+SS AOI model). (For interpretation of the references to color in this figure legend, the reader is referred to the web version of this article.)

Table 11
Number of segments in each section that are expected (manually), predicted based on the raw intensities $I^s_{r,j,k}$, predicted based on the compensated intensities $I^s_{\mathrm{MCI},j,k}$ and the improvement between raw and compensated intensities.

Section	Expected	$I^s_{r,j,k}$	$I^s_{\mathrm{MCI},j,k}$	Imp. [%]
Window	8	36	15	75
Floor	108	165	103	91

results in more meaningful segments that better adhere to the object boundaries within the scene. For example, in Figs. 11(a) and 11(b), we see that each window shutter and the upper wall are represented with one segment each if we use $I^s_{\mathrm{MCI},j,k}$ values, while the same entities are separated in multiple less meaningful segments if we use $I^s_{r,j,k}$. Similarly, in Figs. 11(c) and 11(d), we see that most floor tiles get segmented as single individual segments when using $I^s_{\mathrm{MCI},j,k}$, while the segmentation relying on $I^s_{r,j,k}$ already fails to separate the mortar and the tiles.

To quantify the benefit of the radiometric calibration, we compared the number of estimated segments using both $I^s_{r,j,k}$ and $I^s_{\mathrm{MCI},j,k}$ against the expected number of segments based on the visual identification of separate elements within the scene. Table 11 summarizes this information for both scenes and shows that the number of segments in both cases is smaller and closer to the expected number of segments if we use $I^s_{\mathrm{MCI},j,k}$.

Hence, this simple analysis demonstrates, quantitatively and qualitatively, that the $I^s_{\mathrm{MCI},j,k}$ can be helpful for the point cloud segmentation task. This improvement is primarily caused by the more homogeneous $I^s_{\mathrm{MCI},j,k}$ values related to one material if we compare them relative to raw intensity values.

5.7. Benefit for data integration

Additionally, we want to demonstrate the potential of leveraging $I^s_{\mathrm{MCI},j,k}$ to align the intensities of different instruments. This alignment enables seamless merging of point clouds and using the intensity data for downstream tasks, such as segmentation without requiring knowledge of the reflectances.

In a scanning project that involves multiple scanners, the raw intensity values $I^s_{r,j,k}$ from different scanners can vary significantly. This variation is because $I^s_{r,j,k}$ comprises the system constant $\kappa^s_{R_0}$, AOI function $f^{\mathrm{mat}_j}_{\varphi_0}(\varphi_{j,k})$, and distance function $g^s_{R_0}(R_{j,k})$, which differ across

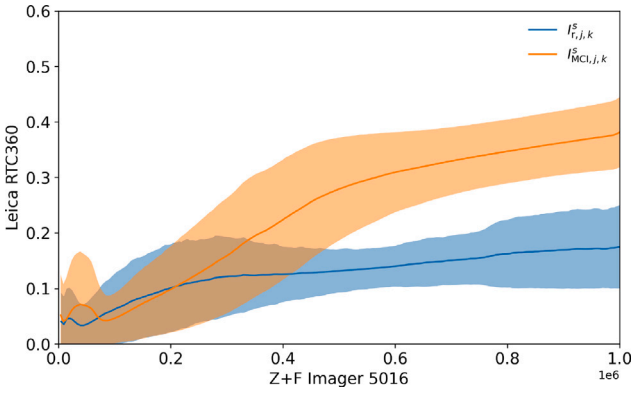

Fig. 12. Relation of $I^s_{r,j,k}$ and $I^s_{\mathrm{MCI},j,k}$ of Z+F Imager 5016 and Leica RTC360. (Dataset 2, AL+SS AOI model). (For interpretation of the references to color in this figure legend, the reader is referred to the web version of this article.)

scanners and measurement configurations. In contrast, when using $I^s_{\mathrm{MCI},j,k}$, the values of $I^s_{\mathrm{MCI},j,k}$ from various scanners differ only in terms of $\kappa^s_{R_0}$ because we already compensated for $f^{\mathrm{mat}_j}_{\varphi_0}(\varphi_{j,k})$ and $g^s_{R_0}(R_{j,k})$. Since $\kappa^s_{R_0}$ is a constant specific to each scanner, we can calculate the ratio of the $\kappa^s_{R_0}$ between two scanners, allowing us to convert the $I^s_{\mathrm{MCI},j,k}$ from one scanner's definition to another's. This ratio can be determined by utilizing scan overlaps. By identifying close points in the point clouds acquired by the different scanners, we can assume that the reflectance of these nearby points remains consistent. This assumption enables us to calculate the ratio of the $\kappa^s_{R_0}$ of two scanners.

To demonstrate the potential for alignment between the scanners, we utilized all scans from Dataset 2 obtained from the Z+F Imager 5016 and the Leica RTC360. To decrease the data volume, we first merged the point clouds from the Leica RTC360 and subsampled it spatially to a resolution of 1 cm. To transfer the Z+F Imager 5016 $I^{\mathrm{Z+F}}_{\mathrm{MCI},j,k}$ into the Leica RTC360 $I^{\mathrm{Leica}}_{\mathrm{MCI},j,k}$, we identified the nearest neighbor in the Z+F Imager 5016 point cloud for each point in the Leica RTC360 point cloud. We excluded corresponding points more than 5 cm apart to ensure that the reflectance values of both points are similar.

Using the corresponding points, we can relate the intensity values $I^{\mathrm{Z+F}}_{r,j,k}$ to $I^{\mathrm{Leica}}_{r,j,k}$ and $I^{\mathrm{Z+F}}_{\mathrm{MCI},j,k}$ to $I^{\mathrm{Leica}}_{\mathrm{MCI},j,k}$, as visualized in Fig. 12, where the $I^s_{r,j,k}$ relation is represented by the blue line and the $I^s_{\mathrm{MCI},j,k}$ relation by the orange line. The $I^s_{\mathrm{MCI},j,k}$ relation demonstrates a stronger correlation than the $I^s_{r,j,k}$ relation, as Spearman's correlation coefficient for the $I^s_{\mathrm{MCI},j,k}$ relation is 0.79, which is higher than the 0.71 observed for the $I^s_{\mathrm{MCI},j,k}$ relation. This suggests that transforming the intensities using the $I^s_{\mathrm{MCI},j,k}$ yields more precise results.

The $I^s_{\mathrm{MCI},j,k}$ relation is not linear, which we would not expect if only the system constant is different for both $I^s_{\mathrm{MCI},j,k}$ systems. Possible reasons can be that (i) the APD of one scanner is not linear, (ii) the $I^s_{\mathrm{MCI},j,k}$ are not entirely independent of the measurement configuration, and (iii) we cannot make the assumption of similar reflectance within 5 cm.

To convert the intensities from the Z+F Imager 5016 to the Leica RTC360, we employed the relation depicted in Fig. 12 as a look-up table. We calculated the median intensity for the Leica RTC360 and the transformed intensities of the Z+F Imager 5016 across four different areas in Dataset 2 that were defined in Section 5.1. To assess the effectiveness of this transformation, we computed the differences between the intensities of the Leica RTC360 and the transformed ones from the Z+F Imager 5016. The results are summarized in Table 12, which presents both the differences and the absolute intensities of the Leica RTC360.

Our analysis revealed that the differences between the $I^s_{\mathrm{MCI},j,k}$ are considerably smaller than those of the $I^s_{r,j,k}$. When compared to the

Table 12
Leica RTC360 intensities for four different areas and the difference of these intensities and the transformed Z+F Imager 5016 intensities once with the raw intensity and once with the compensated intensity.
(Dataset 2, AL+SS AOI model).

Area	$I^{\text{Leica}}_{r,j,k}$	$I^{\text{Leica}}_{\text{MCI},j,k}$	$I^{\text{Leica}}_{r,j,k} - t(I^{\text{ZF}}_{r,j,k})$	$I^{\text{Leica}}_{\text{MCI},j,k} - t(I^{\text{ZF}}_{\text{MCI},j,k})$
Plaster facade	0.416	0.446	0.249	−0.008
Wooden facade	0.024	0.037	−0.014	−0.007
Asphalt	0.145	0.351	−0.028	−0.020
Metallic container	0.376	0.430	0.220	0.005

absolute intensities of the Leica RTC360, the differences in $I^{s}_{r,j,k}$ are between 19% and 70%. In contrast, the differences in $I^{s}_{\text{MCI},j,k}$ are notably smaller, falling between 1% and 23%. This enhanced performance can largely be attributed to the measurement configuration independence, which does not apply to $I^{s}_{r,j,k}$.

In conclusion, our findings demonstrate the potential of $I^{s}_{\text{MCI},j,k}$ for aligning intensity data across different scanners with just one additional computational step, utilizing already available data. This approach allows intensity analysis for multiple scanners for further applications, such as segmentation.

6. Discussion

The presented results demonstrated effective mitigation of measurement configuration related effects on the measured intensities, contributing to obtaining more material-specific values. However, four topics require further discussion: cost-effective use of the method within a typical scanning project (project economy), clarifying a distinction between reflectance coefficients and $I^{s}_{\text{MCI},j,k}$ values, limitations, and transferability of the developed method.

Project economy: In our experiments, scans were captured at a higher scan-station density (and consequently with higher scan overlap) than typically required for standard projects. The median number of overlapping scans falling within individual point cloud patches used in our calculations ranged from 4 to 19, with a minimal requirement of having 3 overlapping scans per patch. Based on our observations, the proposed method should still perform well if a sufficiently large part of the scanned scene is covered by at least three overlapping scans. We find this requirement easily obtainable, especially considering the growing use of cloud-to-cloud registration, which relies on high overlap, and the increasing speed of modern scanners, which minimizes the effort. However, determining the optimal number and distribution of point cloud patches within the scene, optimal number of scans per patch, and the ideal patch size for robust estimation remain open questions. Addressing these parameters in the future will be necessary to aid wider adoption of the method in practical applications.

Reflectance coefficients vs. $I^{s}_{\text{MCI},j,k}$: There are two distinct differences between reflectance coefficients, typically denoted as ρ, and the introduced $I^{s}_{\text{MCI},j,k}$. First, the reflectance is functionally dependent on the incidence angle, hence, not measurement configuration independent, or it refers to the reflectance at 0 deg incidence angle, where the value is dominated by the eventual surface/specular reflection and less related to material properties. Second, estimating reflectance coefficient requires determining instrument-specific constant $\kappa^{s}_{R_0}$ (see Section 5.3), which cannot be resolved within an arbitrary scene without reflectance standards. We opted to calculate $I^{s}_{\text{MCI},j,k}$ rather than reflectance coefficients because we aimed to derive values that are more material-specific. Additionally, we wanted to avoid imposing special requirements for the use of the proposed method, such as obtaining additional scanner parameters from manufacturers or additionally scanning spectral reference targets with known reflectance. Hence, the presented approach circumvents these dependencies, making it more broadly applicable to various scanners and datasets, including legacy data from past scanning projects. If reflectance coefficients are required, they can still be easily obtained from $I^{s}_{\text{MCI},j,k}$ values.

Limitations: Despite its advantages, the proposed method has certain limitations. Due to the correlation between distance and AOI in typical scanning datasets, it remains uncertain whether the fitted functions $f\varphi_0{}^{\text{mat}j}(\varphi j, k)$ and $g^{s}_{R_0}(R_{j,k})$ fully disentangle their respective effects, or whether some degree of cross-influence persists. We did not explicitly control for overfitting, as avoiding it may be less critical for the intended use case, the in-situ radiometric calibration, and achieving consistent intensities across point clouds within the same dataset that was used for the calibration. Nonetheless, future research could benefit from further investigating this issue, and incorporating regularization techniques to enhance the robustness of the estimated functions.

Transferability: The proposed method shows promise for adaptation to mobile and low-cost LiDAR systems, such as those used in automotive applications or small-scale UAVs. To ensure a successful transfer, future adaptations would need to account for systematic differences between beams in multi-beam systems and mitigate the effects of varying line-of-sight conditions (e.g., due to weather, dust, or lens contamination). Moreover, extending the method to these applications presents opportunities, as larger datasets—especially those aggregated from multiple vehicles or platforms—could enable the use of machine learning approaches, complementing or even surpassing the handcrafted methods discussed here. Exploring these extensions remains a key direction for future work.

7. Conclusion

This study presents an automated in-situ radiometric calibration method for TLS, which yields measurement-configuration independent intensities $I^{s}_{\text{MCI},j,k}$ for scanner s, measured point j and scanner station k. Unlike current methods that address the effects of measurement configuration on intensities — often relying on laboratory experiments with dedicated targets (reflection standards), partially manual processing, and task-specific solutions — our method utilizes overlapping point clouds collected during a scanning project (if some conditions are met) without the need for specialized equipment. To determine the $I^{s}_{\text{MCI},j,k}$, we estimated an AOI function $f^{\text{mat}_j}_{\varphi_0}(\varphi_{j,k})$ and a distance function $g^{s}_{R_0}(R_{j,k})$.

The first part of our method involves compensating most of the measurement configuration related effect on intensity values in a globally optimal way for the entire point cloud. This approach effectively reduces the bias in intensities captured from different scan stations while sampling the same material. Our global compensation method outperforms comparable state-of-the-art methods with the abovementioned characteristics. Furthermore, we demonstrate that our method is generalizable across various scenes and different instruments by testing it on three distinct datasets captured with multiple scanners.

Additionally, since each material exhibits different backscattering characteristics, using a single global function $f^{\text{glob}}_{\varphi_0}(\varphi_{j,k})$ to perfectly compensate for all materials is impossible. To account for that, we propose an extension that estimates AOI functions for each material individually to reduce further biases in intensity values caused by varying material characteristics. Besides improving the $I^{s}_{\text{MCI},j,k}$ values, these material-specific functions $f^{\text{mat}_j}_{\varphi_0}(\varphi_{j,k})$ can later be utilized for material probing.

Finally, through a small demonstration, we show that using $I^{s}_{\text{MCI},j,k}$ instead of raw intensities can improve the segmentation of point clouds. Furthermore, we demonstrate the benefit of using $I^{s}_{\text{MCI},j,k}$ for data integration in projects that involve multiple scanners. By leveraging the computed $I^{s}_{\text{MCI},j,k}$ values of each scanner and existing overlaps between point clouds from different scanners, we can establish a relation between the $I^{s}_{\text{MCI},j,k}$ of different scanners. This relation enables us to transfer the $I^{s}_{\text{MCI},j,k}$ values from one scanner to another. With this capability for transferability, we can employ point clouds from various scanners for further downstream tasks.

In summary, our automated in-situ radiometric calibration method effectively compensates for measurement configuration effects in TLS

data. By reducing the measurement configuration effect on intensity measurements, improving the segmentation of point clouds, and enabling consistent data integration across different scanners, this method enhances the utility of TLS intensity values for various applications in remote sensing.

CRediT authorship contribution statement

H. Laasch: Writing – review & editing, Formal analysis, Validation, Methodology, Writing – original draft, Software, Data curation, Investigation, Conceptualization, Visualization. **T. Medic:** Methodology, Writing – review & editing, Conceptualization, Supervision. **N. Pfeifer:** Supervision, Writing – review & editing, Methodology. **A. Wieser:** Methodology, Conceptualization, Funding acquisition, Supervision, Writing – review & editing.

Declaration of Generative AI and AI-assisted technologies in the writing process

During the preparation of this work the authors used ChatGPT-4o and Grammarly in order to improve readability and language. After using this tools, the authors reviewed and edited the content as needed and take full responsibility for the content of the publication.

Declaration of competing interest

The authors declare that they have no known competing financial interests or personal relationships that could have appeared to influence the work reported in this paper.

Acknowledgments

This work was supported by the ETH Research Grant “Protect Sandstone Monuments”. Additionally, we want to thank Markus Mettenleiter of the company Z+F for answering our questions about laser scanners.

References

Bai, J., Niu, Z., Gao, S., Bi, K., Wang, J., Huang, Y., Sun, G., 2023. An exploration, analysis, and correction of the distance effect on terrestrial hyperspectral LiDAR data. ISPRS J. Photogramm. Remote Sens. 198, 60–83.

Bai, J., Niu, Z., Wang, L., 2024. A theoretical demonstration on the independence of distance and incidence angle effects for small-footprint hyperspectral LiDAR: Basic physical concepts. Remote Sens. Environ. 315, 114452.

Blinn, J.F., 1977. Models of light reflection for computer synthesized pictures. SIGGRAPH Comput. Graph. 11 (2), 192–198.

Bretagne, E., Dassonvalle, P., Caron, G., 2018. Spherical target-based calibration of terrestrial laser scanner intensity. Application to colour information computation. ISPRS J. Photogramm. Remote Sens. 144, 14–27.

Carrea, D., Abellan, A., Humair, F., Matasci, B., Derron, M.-H., Jaboyedoff, M., 2016. Correction of terrestrial LiDAR intensity channel using Oren–Nayar reflectance model: An application to lithological differentiation. ISPRS J. Photogramm. Remote Sens. 113, 17–29.

Dierckx, P., 1975. An algorithm for smoothing, differentiation and integration of experimental data using spline functions. J. Comput. Appl. Math. 1 (3), 165–184.

Efron, B., 1982. The Jackknife, the Bootstrap and Other Resampling Plans. Society for Industrial and Applied Mathematics.

Elsherif, A., Gaulton, R., Mills, J., 2018. Estimation of vegetation water content at leaf and canopy level using dual-wavelength commercial terrestrial laser scanners. Interface Focus. 8 (2), 20170041.

Errington, A.F.C., Daku, B.L.F., Prugger, A.F., 2015. Reflectance modelling using terrestrial LiDAR intensity data. In: 2015 IEEE International Conference on Imaging Systems and Techniques. IST, pp. 1–6.

Errington, A.F.C., Daku, B.L.F., Prugger, A.F., 2016. Clay mapping in underground potash mines: An initial investigation into the use of corrected intensity terrestrial LiDAR data. In: 2016 IEEE International Conference on Imaging Systems and Techniques. IST, pp. 94–99.

Hackel, T., Wegner, J.D., Schindler, K., 2016. Contour detection in unstructured 3D point clouds. In: 2016 IEEE Conference on Computer Vision and Pattern Recognition. CVPR, pp. 1610–1618.

Han, Y., Salido-Monzú, D., Wieser, A., 2022. Comb-based multispectral LiDAR providing reflectance and distance spectra. Opt. Express 30 (23), 42362–42375.

Harintaka, H., Wijaya, C., 2024. Improved deep learning segmentation of outdoor point clouds with different sampling strategies and using intensities. Open Geosci. 16 (1), 20220611.

Hastie, T., Tibshirani, R., Friedman, J., 2009. The Elements of Statistical Learning: Data Mining, Inference, and Prediction. In: Springer series in statistics, Springer.

Janßen, J., Kuhlmann, H., Holst, C., 2021. Assessing the temporal stability of terrestrial laser scanners during long-term measurements. In: Contributions To International Conferences on Engineering Surveying. pp. 69–84.

Jelalian, A., 1992. Laser Radar Systems. In: Artech House radar library, Artech House.

Jin, J., Verbeurgt, J., De Sloover, L., Stal, C., Deruyter, G., Montreuil, A.-L., Vos, S., De Maeyer, P., De Wulf, A., 2021. Support vector regression for high-resolution beach surface moisture estimation from terrestrial LiDAR intensity data. Int. J. Appl. Earth Obs. Geoinf. 102, 102458.

Kaasalainen, S., Ahokas, E., Hyyppa, J., Suomalainen, J., 2005. Study of surface brightness from backscattered laser intensity: Calibration of laser data. IEEE Geosci. Remote. Sens. Lett. 2 (3), 255–259.

Kaasalainen, S., Jaakkola, A., Kaasalainen, M., Krooks, A., Kukko, A., 2011. Analysis of incidence angle and distance effects on terrestrial laser scanner intensity: Search for correction methods. Remote. Sens. 3 (10), 2207–2221.

Kaasalainen, S., Niittymaki, H., Krooks, A., Koch, K., Kaartinen, H., Vain, A., Hyyppa, H., 2010. Effect of target moisture on laser scanner intensity. IEEE Trans. Geosci. Remote Sens. 48 (4), 2128–2136.

Kashani, A., Olsen, M., Parrish, C., Wilson, N., 2015. A review of LIDAR radiometric processing: From ad hoc intensity correction to rigorous radiometric calibration. Sensors 15 (11), 28099–28128.

Laasch, H., Medic, T., Wieser, A., 2023. Towards assessing sandstone surface moisture and degradation level from radiometrically corrected TLS intensity data. In: ISPRS Annals of the Photogrammetry, Remote Sensing and Spatial Information Sciences. vol. X-1/W1-2023, pp. 567–574.

Lambert, J.H., 1760. Photometria sive de mensura et gradibus luminis, colorum et umbrae. In: Photometria sive de mensura et gradibus luminis, colorum et umbrae. Augustae Videlicorum: sumptibus viduae Eberhardi Klett typis Chistophori Petri Detleffsen.

Li, X., Shang, Y., Hua, B., Yu, R., He, Y., 2023. LiDAR intensity correction for road marking detection. Opt. Lasers Eng. 160, 107240.

Li, X., Yu, R., Bi, T., Xu, L., 2024. A traffic sign classification method using LiDAR corrected intensity and geometric feature. IEEE Sensors J. 24 (7), 11796–11804.

Maru, M.B., Wang, Y., Kim, H., Yoon, H., Park, S., 2023. Improved building facade segmentation through digital twin-enabled RandLA-Net with empirical intensity correction model. J. Build. Eng. 78, 107520.

Oren, M., Nayar, S.K., 1994. Seeing beyond Lambert’s law. In: Eklundh, J.-O. (Ed.), Computer Vision — ECCV ’94. Springer Berlin Heidelberg, pp. 269–280.

Pfeifer, N., Dorninger, P., Haring, A., Fan, H., 2007. Investigating terrestrial laser scanning intensity data: quality and functional relations. 8th Conf. Opt. 3- D Meas. Tech. 328–337.

Pfeifer, N., Höfle, B., Briese, C., Rutzinger, M., Haring, A., 2008. Analysis of the backscattered energy in terrestrial laser scanning data. In: Proceedings of the XXI Congress: Silk Road for Information from Imagery: 3-11 July, Beijing, China. International Society for Photogrammetry and Remote Sensing (ISPRS), pp. 1045–1051.

Pfreundschuh, P., Oleynikova, H., Cadena, C., Siegwart, R., Andersson, O., 2024. Coinlio: Complementary intensity-augmented lidar inertial odometry. In: 2024 IEEE International Conference on Robotics and Automation. ICRA, IEEE, pp. 1730–1737.

Poullain, E., Garestier, F., Bretel, P., Levoy, F., 2012. Modeling of als intensity behavior as a function of incidence angle for coastal zone surface study. In: 2012 IEEE International Geoscience and Remote Sensing Symposium. pp. 2849–2852.

Sanchiz-Viel, N., Bretagne, E., Mouaddib, E.M., Dassonvalle, P., 2021. Radiometric correction of laser scanning intensity data apllied for terrestrial laser scanning. ISPRS J. Photogramm. Remote Sens. 172.

Tan, K., Chen, J., Qian, W., Zhang, W., Shen, F., Cheng, X., 2019. Intensity data correction for long-range terrestrial laser scanners: A case study of target differentiation in an intertidal zone. Remote. Sens. 11 (3), 331.

Tan, K., Chen, J., Zhang, W., Liu, K., Tao, P., Cheng, X., 2020. Estimation of soil surface water contents for intertidal mudflats using a near-infrared long-range terrestrial laser scanner. ISPRS J. Photogramm. Remote Sens. 159, 129–139.

Tan, K., Cheng, X., 2015. Intensity data correction based on incidence angle and distance for terrestrial laser scanner. J. Appl. Remote. Sens. 9 (1), 094094.

Viswanath, K., Jiang, P., Sujit, P., Saripalli, S., 2023. Off-road lidar intensity based semantic segmentation. In: International Symposium on Experimental Robotics. Springer, pp. 608–617.

Wei Fang, Xianfeng Huang, Fan Zhang, Deren Li, 2015. Intensity correction of terrestrial laser scanning data by estimating laser transmission function. IEEE Trans. Geosci. Remote Sens. 53 (2), 942–951.

Xiang, B., Yue, Y., Peters, T., Schindler, K., 2023. A review of panoptic segmentation for mobile mapping point clouds. ISPRS J. Photogramm. Remote Sens. 203, 373–391.

Xu, C., Wu, B., Wang, Z., Zhan, W., Vajda, P., Keutzer, K., Tomizuka, M., 2020. Squeeze-SegV3: Spatially-adaptive convolution for efficient point-cloud segmentation. In: Vedaldi, A., Bischof, H., Brox, T., Frahm, J.-M. (Eds.), Computer Vision – ECCV 2020. Springer International Publishing, pp. 1–19.

Zhan, Q., Liang, Y., Xiao, Y., 2009. Color-based segmentation of point clouds. Laser Scanning 38 (3), 155–161.

Zhang, Y., Zhou, Z., David, P., Yue, X., Xi, Z., Gong, B., Foroosh, H., 2020. Polarnet: An improved grid representation for online lidar point clouds semantic segmentation. In: Proceedings of the IEEE/CVF Conference on Computer Vision and Pattern Recognition. pp. 9601–9610.